

## Chapter 7

# Photocathodes

Wei Liu<sup>1,2,3</sup>, Matt Poelker<sup>3</sup>, John Smedley<sup>4</sup>, Romain Ganter<sup>5</sup>

<sup>1</sup>*Institute of Modern physics, Chinese Academy of Sciences, 509 Nanchang Rd., Lanzhou, 730000, China,*

<sup>2</sup>*University of Chinese Academy of Sciences, 19A Yuquan Rd., Beijing, 100049, China*

<sup>3</sup>*Thomas Jefferson National Accelerator Facility, 12000 Jefferson Avenue, Newport News, Virginia, 23606, USA; email Wei Liu: [wliu@bnl.gov](mailto:wliu@bnl.gov); email Matt Poelker: [poelker@jlab.org](mailto:poelker@jlab.org)*

<sup>4</sup>*Los Alamos National Laboratory, New Mexico 87545, USA; email: [smedley@lanl.gov](mailto:smedley@lanl.gov)*

<sup>5</sup>*Paul Scherrer Institut, 5232 Villigen PSI, Switzerland; email: [romain.ganter@psi.ch](mailto:romain.ganter@psi.ch)*

**Abstract** Photocathodes were at the heart of quantum physics development in the early twentieth century and are still used in high technologies devices like night-vision goggles, photomultiplier tubes and particle accelerators. The simplest form of photocathode is a metallic surface, negatively biased, from which electrons are extracted by energetic photons. After a brief description of the photocathode preparation, this chapter will present the latest developments and limitations of metallic and semiconductor photocathodes.

## Contents

7.1	Introduction to photoemission .....	4
7.1.1	One-Step and Three-Step Models of Photoemission .....	4
7.1.2	Comparison between metal and semiconductor photoemission processes based on the three-step model .....	5
7.1.3	Importance of the Density of States.....	6
7.2	Metallic Photocathodes: .....	8
7.2.1	Introduction:.....	8
7.2.2	Practical approach to photoemission from metals .....	8
7.2.3	QE performances of metals.....	10
7.2.4	Limitations and potential of metallic photocathodes .....	14
	Cathode preparation: bulk material choice, polishing and cleaning techniques.....	14
	Incident photons .....	19
	Surface Electric Field: .....	20
	Superconducting photocathodes: .....	22
7.3	Positive Electron Affinity Semiconductors .....	23
7.3.1	Introduction.....	23
7.3.2	Preparation and performance of Cs <sub>2</sub> Te photocathodes: .....	24
	Preparation methods .....	24
	QE values of Alkali based cathodes - Cs <sub>2</sub> Te: .....	25
7.3.3	Sensitivity to vacuum .....	26
7.3.4	Alkali-Antimonide photocathodes:.....	27
	Preparation methods and film properties.....	28
	<i>In situ</i> x-ray analysis during growth.....	29
7.4	NEA Semiconductors: GaAs based photocathodes for polarized electron beams .....	30
7.4.1	Overview of GaAs photocathodes.....	30
7.4.2	Theory: Spin relaxation mechanisms.....	33
7.4.3	Recent Measurements with GaAs NEA Photocathodes .....	34
	Bulk GaAs Polarization Study - Temperature and Dopant Dependence .....	34
	High Polarization Strained-Superlattice Photocathode with Distributed Bragg Reflector.....	37
	Ion Bombardment – Cleave Plane Dependence.....	41
	Conclusion .....	48
	References.....	49

Figure captions ..... 53

## 7.1 Introduction to photoemission

### 7.1.1 One-Step and Three-Step Models of Photoemission

Photoemission has a long and storied history in physics, beginning with Einstein's explanation of the photoelectric effect in 1905. Today photoemission spectroscopy, both in the UV and X-ray regime (UPS/XPS), is used to characterize materials, determine chemical bonding and measure electronic band structures of materials. Two prevailing theoretical frameworks exist for describing photoemission, the one-step quantum mechanical model [1], and the **three-step model** [1,2] described in detail below. The one-step model relies on a "sudden" approximation, where electrons are excited from a bound state within a material to a free state outside of it, in a transition that can be described by a quantum mechanical matrix element. This model is widely used in UPS analysis to understand material band structure; it considers electrons to conserve both energy and momentum upon emission. While powerful, this model is in general not widely applicable to practical photocathodes, as it generally assumes well defined crystalline initial states, and ignores electron scattering within the material.

The Three-Step Model was developed to deal with photoemission in practical photocathodes, and had found great success in predicting the behavior of both metals and semiconductors in the near-threshold regime that dominates most applications. In this model, the process is broken into:

1. absorption and excitation
2. transport to surface
3. escape over or through the surface barrier

Step 1 accounts for loss of incident light due to reflection, and the excitation of electrons from filled states in the material valence band to excited states in the material conduction band. Most treatments of the model neglect momentum as a conserved quantity, reasoning that phonon scattering and the polycrystalline initial state will randomize the electron momentum state while leaving its energy largely unaffected. The **electronic Density of States** (DOS) is considered, so conservation of energy is accounted for. In this way, the model accounts for unproductive absorption (photons which excite electrons to conduction band states with energy below the vacuum level, so that they cannot escape).

Step 2 accounts for loss due to the various scattering processes which occur during the transport to the surface. Here the photon absorption length is compared to the electron mean free path, to determine the fraction of electrons lost to scattering. For metals, the dominant scattering mechanism is electron-electron scattering, and a single scattering event is considered to be a loss mechanism. For semiconductors, as will be discussed in detail later, **electron-electron scattering** is often forbidden and other scattering mechanisms take over.

Step 3 accounts for the direction of travel within the material as the electron approaches the surface. Although we often think of the **work function** as a limit on the energy required to escape the material, it is actually a limit on required momentum perpendicular to the material surface. Thus, the electron direction of travel must be within a cone defined by the energy in excess of the minimum energy needed to escape. For metals, failure to meet this criterion is considered a loss mechanism, as the electron will reflect off the surface and be lost to subsequent e-e scattering. For semiconductors, a

Monte Carlo treatment is required, as the electrons may have their direction of travel randomized again via phonon scattering.

Each step represents a probability of photon/electron survival. The product of these probabilities, taking angular considerations into account where appropriate, yields a **energy distribution curve** (EDC) that represents the probability per unit range of total-energy (measured relative to the top of the barrier) that an incident photon of specified wavelength will produce (at the cathode surface) an electron that will escape from the surface. The integration of this EDC over all energies above the barrier energy level (also called the "**threshold level**") yields the **quantum efficiency** (QE), that is the ratio of the number of emitted electrons emitted to the number of incident photons.

### 7.1.2 Comparison between metal and semiconductor photoemission processes based on the three-step model

Metal photocathodes are used for some accelerator applications that need only low average current, especially where prompt response time is required. However, most new accelerator applications and virtually all photo-detector applications use semiconductor cathodes. The reason for this is that semiconductor cathodes offer far superior quantum efficiency performance, and can be sensitive to visible or infrared radiation. The photoemission mechanism for both **metals** and **semiconductors** can be described by the three step model outlined above [3]. However, there are two fundamental differences – the extent of unproductive absorption and the type of collisions that photoexcited electrons experience during their travel to the surface.

In metals, photons can in general be absorbed throughout the conduction band, resulting in a large number of photons being “used” to excite electrons to states that lack sufficient energy to escape. In addition, photoexcited electrons may collide with electrons from the conduction band. In such scattering, the photoexcited electrons lose energy such that they can no longer escape (Fig. 7.1) and thus will not contribute to the QE. In consequence, only electrons within one **electron mean free path**  $\lambda_{e-e}$  below the surface can possibly escape. In metals, the value of  $\lambda_{e-e}$  is much smaller than the laser penetration depth so only a small fraction of the photoexcited electrons can be emitted (the violet area in Fig. 7.1) making the QE of metals low.

In semiconductors, the bandgap performs two functions. First, it limits unproductive absorption, as no electrons are excited into the bandgap due to the absence of a final allowed state. The lack of states in the band gap also has a consequence on scattering – electron-electron collisions are not allowed if the final energy of electrons falls into this gap (Fig. 7.1). As a consequence,  $\lambda_{e-e}$  can be even larger than the laser penetration depth and all photoexcited electrons could potentially reach the surface. This makes the QE of semiconductors much larger than the QE of metals [4], since the reservoir of electrons eligible for photoemission is much larger than for metals. For example, the forbidden gap of Cs<sub>2</sub>Te photocathodes is 3.3 eV wide. Only the electrons excited above an energy of 6.6 eV will be able to scatter with an electron from the valence band. With laser light at 266 nm (i.e., a photon energy of 4.6 eV), photoexcited electrons will not interact with the other electrons from the conduction band during their travel to the surface. Other scattering processes, such as grain boundary scattering and scattering with lattice phonons still occur; however electrons in these interactions tend to lose only a small fraction of their energy [5]. Scattering of electrons with the lattice can even be beneficial, as the interaction randomizes the electron momentum with minimal loss of energy. This allows electrons that

are initially moving away from the surface to be redirected, potentially allowing emission. In this way, semiconductor cathodes can have a QE over 50 % (cesium iodide, for example). Interaction with the lattice can also cool the electrons, which is beneficial for certain accelerator photoinjector applications, as it reduces the total initial kinetic energy of the photoemitted electrons ( $E_{kin}$ ) and thus also the intrinsic emittance.

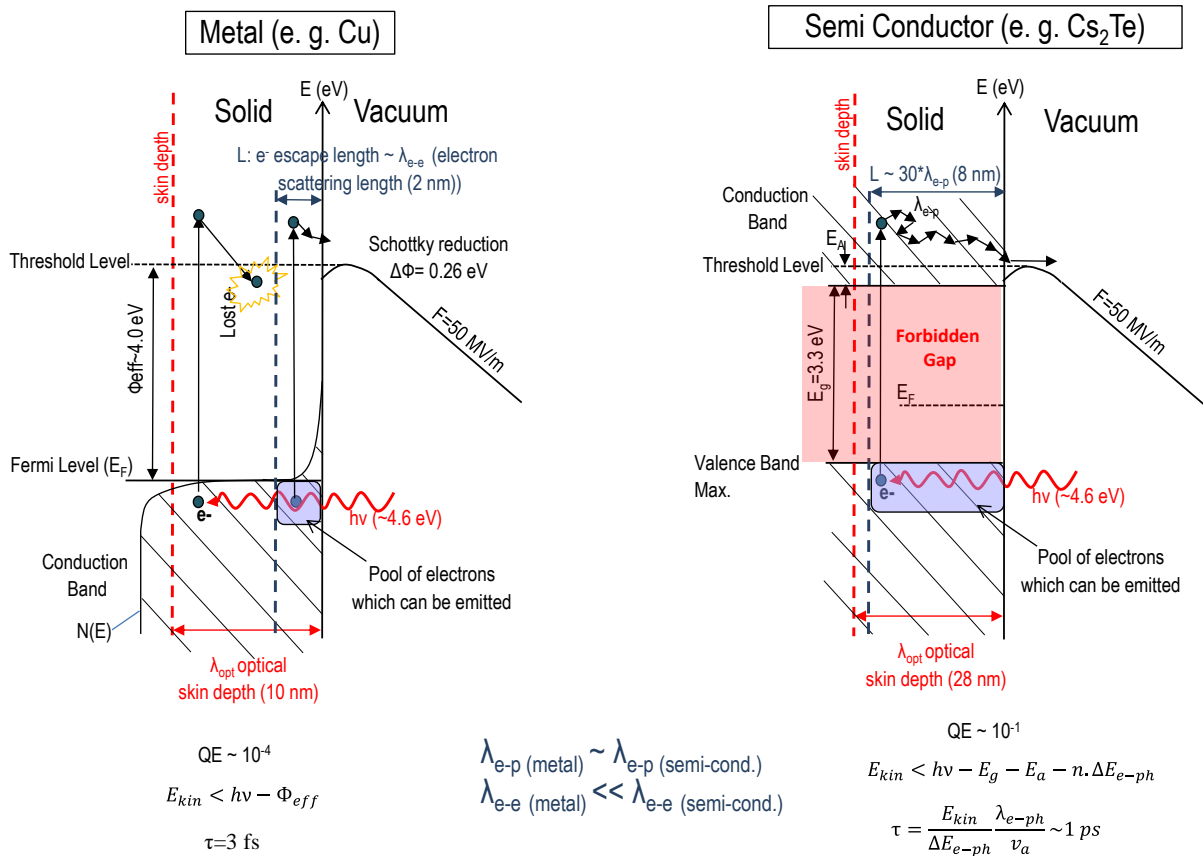


**Fig. 7.1** The three step model of photoemission can be used both for metals and semiconductors; here the parameters of copper and Cs<sub>2</sub>Te are compared.  $\lambda_{e-e}$  and  $\lambda_{e-p}$  correspond to the electron mean free path between electron-electron and electron-phonon scattering events;  $\tau$  is the electron extraction time (colored figure). Note that, even if an electron has total-energy  $E$  above the threshold level, it cannot escape unless the energy associated with its motion normal to the surface is also above the threshold level

### 7.1.3 Importance of the Density of States

The **electronic density of states** (DOS),  $N(E)$ , is a function that describes the number of available electron states per unit range in total electron energy  $E$ , per unit volume of material. True densities of states for niobium (Nb) and lead (Pb) are shown in Fig. 7.2. In the simplest model, the so-called "free-electron metal",  $N(E)$  is proportional to  $(E - E_{CB})^{1/2}$ , where  $E_{CB}$  is the energy of the conduction-band base. However, many theoretical implementations of the three-step model ignore the energy dependence in  $N(E)$ . Instead, metals are assumed to have an appropriate constant density of states, and semiconductors are assumed to have an appropriate constant density of states where states exist (i.e., not in the band gap region). This simplifying assumption allows for closed QE calculations such as (7.2) in the next section, and produces reasonable agreement with experimental data for some materials, especially metals that are "free electron"-like. These are typically materials in the first and second

columns of the periodic table, and in the 13<sup>th</sup> and higher (materials that emit electrons from their s or p orbitals). It fails badly for many transition metals, such as niobium. Other transition metals, such as copper, behave as S-band emitters for near-threshold photons.

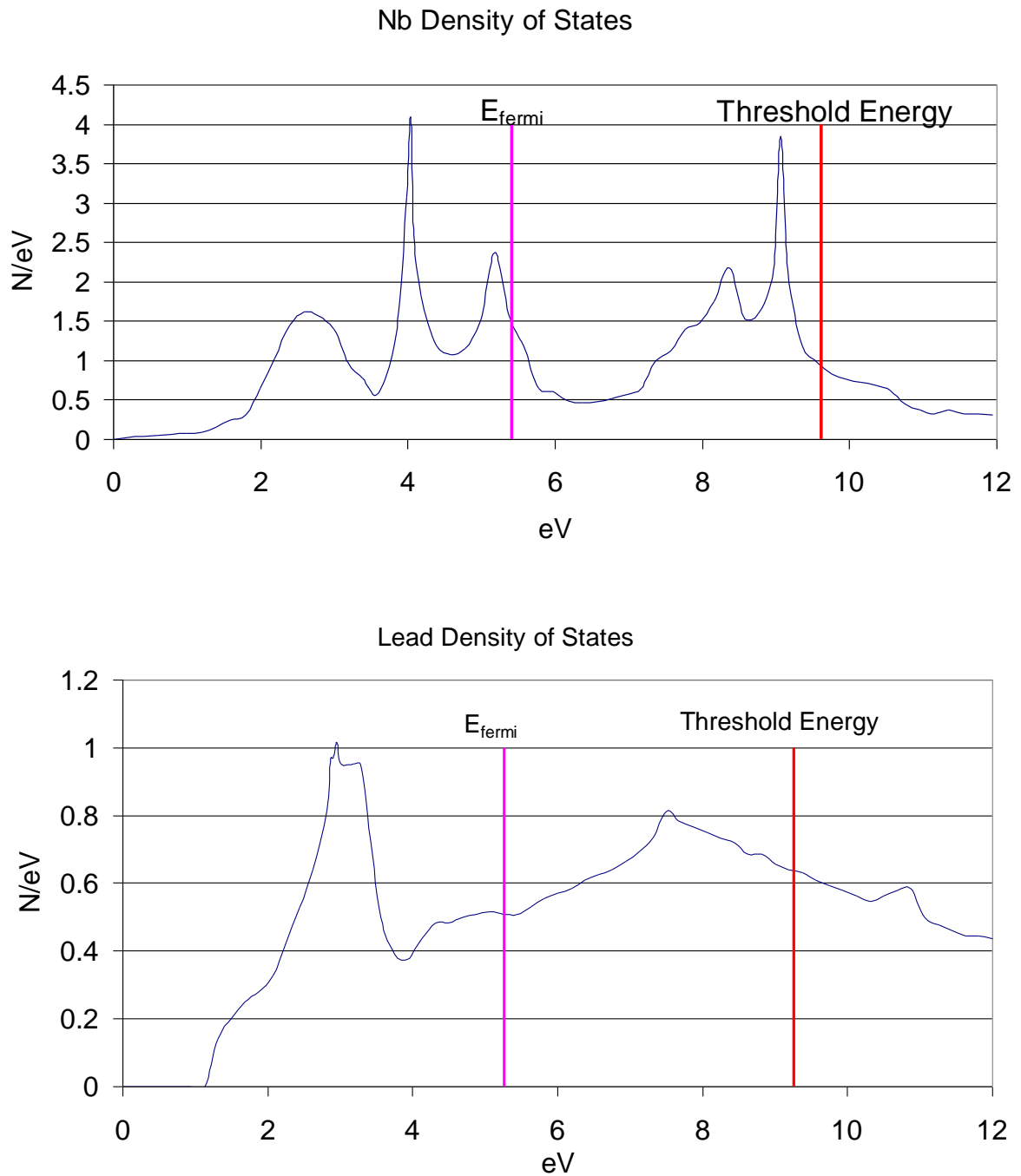


**Fig. 7.2** Densities of states  $N(E)$  for a transition metal (Nb, top) and a p-band emitter (Pb, bottom), as functions of total-energy  $E$  measured from the base of the conduction band. The separation of filled and empty states is labeled by the Fermi energy, and the minimum energy required to escape the material (in the absence of the Schottky effect) is labeled as the threshold energy [6,7] (colored figure). This threshold energy is the sum of the Fermi energy and the work function

## 7.2 Metallic Photocathodes:

### 7.2.1 Introduction:

The metals discussed in this chapter are the most common metals that occur freely in nature. An important characterization parameter for a photocathode is its quantum efficiency (QE), and the goal of many studies is to increase the QE of cathodes. In practice, the QE is not the only parameter to look at, because the QE value obtained under the ideal conditions of a laboratory might not be reproducible in all photocathode applications. Indeed, many other constraints like the work function, the wavelength of incident photons, the applied electric field amplitude, and the mechanical assembly where the cathode sits, will determine the type of cathode material to choose and consequently the QE that can be expected. In the following sections, we will review the most important parameters that determine the performance of a photocathode material.

### 7.2.2 Practical approach to photoemission from metals

For a given illumination wavelength, the QE depends on three fundamental parameters: the photocathode **reflectivity**, the material work function and the applied electric field—see (7.2). **Metallic photocathodes** are often used in applications where the cathode surface has to be exposed to air. Metallic surfaces will not lose much QE after brief exposure to air, although long exposure to humid air can be problematic. Among metallic photocathodes, a well-known and studied example is the **copper photocathode**. The following paragraphs examine in more detail the behavior of copper photocathodes.

Since photoemission is a process taking place in the first tens of nanometers below the surface, it highly depends on the quality of the surface which, unfortunately, is changing with time. For example, the work function of a material depends on the presence of contaminants, but these contaminants might also migrate across the surface over time. Surface contamination (e.g., oxidation) changes the reflectivity of the surface and thus the QE. The electric field applied on the cathode surface will be enhanced depending on the roughness of the surface, which can change with photocathode use. This electric field enhancement will also affect the QE locally, through a field-induced reduction in height of the potential-energy (PE) barrier that prevents electron escape into vacuum. This reduction is due to the **Schottky effect**. At any particular surface location, one can define an “effective local work function” by:

$$\Phi_{eff} = \Phi_0 - \sqrt{\frac{e^3 F}{4\pi\epsilon_0}} \quad (7.1)$$

where  $\Phi_0$  is the conventional (zero-field) local work function,  $e$  the elementary charge,  $\epsilon_0$  the electric constant, and  $F$  is the (positive) magnitude of the (physically negative) local electric field normal to the surface. The schematic of Fig. 7.3 illustrates this link between the fundamental parameters driving the QE and practical aspects of photocathodes.

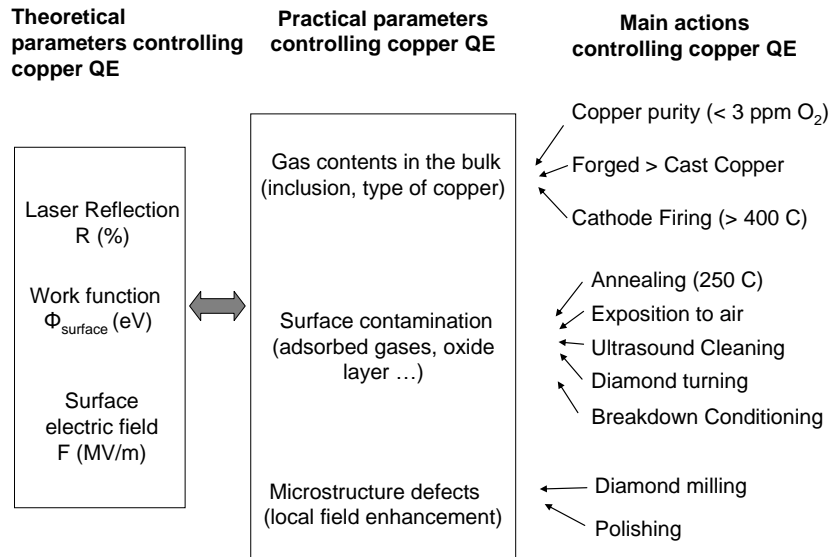


**Fig. 7.3** Schematic representation of the link between the theoretical parameters controlling the QE of copper and macroscopic properties as well as ways to act on these properties

The time varying nature of photocathode QE can be problematic, and sometimes photocathode QE even increases [8], as illustrated in Fig. 7.4, where the photocathode QE increased by more than an order of magnitude after 4 days of operation. This was probably due to cleaning/removal of the contaminants by the illuminating laser. Such a QE variation corresponds, in theory, to only 0.06 eV drop in the surface work function.

Based on the three-step model, and the assumptions that the zero-temperature (step-like) Fermi-Dirac distribution may be used and that (near the threshold total-energy for escape) the DOS may be treated as constant, Dowell et. al. [9] derived a simple expression [their eq. (19)] for the QE of metals:

$$QE(\omega) = \frac{1 - R(\omega)}{1 + \frac{\lambda_{\text{opt}}}{2\lambda_{e-e}(E_m)} \frac{\hbar\omega\sqrt{\Phi_{\text{eff}}}}{E_m^{3/2}} \left(1 + \sqrt{\frac{\Phi_{\text{eff}}}{\hbar\omega}}\right)} \frac{(E_f + \hbar\omega)}{2\hbar\omega} \times \left[1 + \frac{E_f + \Phi_{\text{eff}}}{E_f + \hbar\omega} - 2\sqrt{\frac{E_f + \Phi_{\text{eff}}}{E_f + \hbar\omega}}\right], \quad (7.2)$$

where  $R$  denotes the reflectivity,  $\lambda_{\text{opt}}$  is the laser penetration depth,  $\lambda_{e-e}$  is the mean free path of electrons between two consecutive **electron-electron scattering** events,  $\hbar\omega$  is the photon energy,  $\Phi_{\text{eff}}$  is the effective work function already reduced by the Schottky effect [see (7.1)],  $E_f$  is the Fermi energy [that is, the total-energy difference ( $E_f - E_{\text{CB}}$ ) between the Fermi level ( $E_f$ ) and the base of the conduction band ( $E_{\text{CB}}$ )], and  $E_m$  is the total-energy difference ( $E_m = E_s - E_f$ ) between the total-energy ( $E_s$ ) at which  $\lambda_{e-e}$  has been determined and the Fermi level. Expression (7.2) accurately reproduces the experimental data for copper.

In the measurements shown in Fig. 7.4, it is interesting to note that increasing the electric field from 10 MV/m to 20 MV/m results in a QE increase by a factor 10. Such a doubling of the electric field can easily happen locally, due to mechanically protruding defects that enhance the electric field (**tip effect**) on a microscopic scale. This illustrates the importance of the Schottky effect.

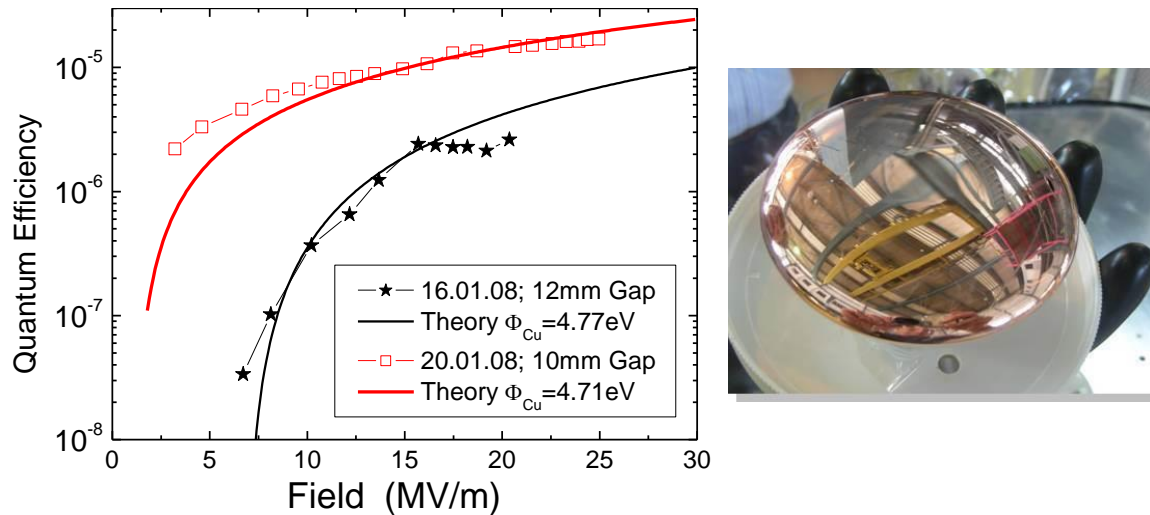


**Fig. 7.4** QE of a copper photocathode versus the applied electric field during 4 days of operation. Laser pulses at 266 nm with 6  $\mu$ J energy per pulse, at 10 Hz repetition rate, were used to illuminate the copper photocathode with quasi-normal incidence. The copper photocathode (inset) was diamond turned, providing an average roughness of a few nanometers. The theoretical curve corresponds to the QE expression (7.2) taken from [9]

Any change of the surface state will modify the three fundamental parameters (reflection, work function and local electric field) at the same time. For example, changes in the method of **polishing** the surface will change the microstructure profile and thus the local electric field, but will also change the reflectivity of the surface, and might also change the density of contaminants (which in turns modifies the local work function).

### 7.2.3 QE performances of metals

Because of the technical difficulty of having atomically clean samples, free of **contaminants**, the QE of a polycrystalline metal can easily vary from one sample to another. In Table 7.1, typical values of QE measured for different transition metals are presented. These values were obtained by laser illumination at different wavelengths on polycrystalline metals. Most of Table 7.1 comes from Suberlucq [10] but is augmented with some recent results. The work function data was compiled by Michaelson [11]. These values correspond to the most reasonable work function values for polycrystalline metals used in practice: the so-called "preferred work function". Since the work function depends on the crystal orientation distribution, the vacuum quality and the **surface cleanliness**, one can reasonably expect a variation of 0.1 – 0.2 eV from one sample to another. This is the reason why QE values differ from one measurement to another in Table 7.1.

**Table 7.1** Quantum Efficiency of polycrystalline metallic photocathodes (main source: [10])

$\lambda$ [nm]	193	213/209	248	262-266	308	355	$\phi_s$	Ref.
$E$ [eV]	6.4	5.8 / 5.9	5	4.7	4	3.5	eV	
Al		$8.4 \cdot 10^{-4}$		$3.2 \cdot 10^{-5}$		$3.4 \cdot 10^{-7}$	4.3	[12] [13]
Ag <sup>(a)</sup>				$2 \cdot 10^{-5}$			4.3	[14]
Ag <sup>(b), (g)</sup>				$8.4 \cdot 10^{-5}$			5.06	[15]
Au <sup>(a)</sup>				$4.7 \cdot 10^{-5}$			5.1	[14]
Au		$4 \cdot 10^{-4}$		$1.310^{-5}$			5.1	[12]
Ca			$4 \cdot 10^{-5}$				2.9	[16]
Cu	$2.0 \cdot 10^{-4}$	$1.5 \cdot 10^{-4}$		$2.2 \cdot 10^{-6}$	$1.6 \cdot 10^{-7}$	$8 \cdot 10^{-9}$	4.6	[12]
Cu <sup>(b)</sup>	$1.5 \cdot 10^{-3}$	$4.2 \cdot 10^{-4}$					4.6	[12]
Cu <sup>(a) (g)</sup>				$1.4 \cdot 10^{-4}$			4.6	[14] & [17] [18]
Cu			$5 \cdot 10^{-5}$					[19] [20]
Mg				$5.1 \cdot 10^{-5}$			3.7	[12]
Mg				$2.7 \cdot 10^{-4}$			3.7	[12]
Mg <sup>(d)</sup>				$5 \cdot 10^{-4}$			3.7	[21]
Mg <sup>(b)</sup>				$1.7 \cdot 10^{-3}$			3.7	[15]
Mo				$< 7 \cdot 10^{-7}$			4.6	[12] [13]
Mo <sup>(b)</sup>				$2.5 \cdot 10^{-6}$			4.6	[15]
Nb	$4.5 \cdot 10^{-4}$		$3.2 \cdot 10^{-6}$				4.3	[22]
Nb				$3 \cdot 10^{-6}$			4.3	[13]
Nb <sup>(b)</sup>				$1.9 \cdot 10^{-4}$			4.3	[15]
Nb <sup>(b), (g)</sup>				$2.6 \cdot 10^{-4}$				[18]
Ni <sup>(a)</sup>				$2.5 \cdot 10^{-5}$			5.2	[14]
Pb	$5.4 \cdot 10^{-3}$	$2.7 \cdot 10^{-3}$					3.88	[7]
Pb <sup>(b)</sup>				$2.2 \cdot 10^{-4}$			3.88	[15]
Pd <sup>(a)</sup>				$1.2 \cdot 10^{-5}$			5.1	[14]
Ac 316 LN		$9 \cdot 10^{-5}$		$1.6 \cdot 10^{-6}$			?	[12]
Sm					$1.6 \cdot 10^{-6}$		2.7	[12]
Sm <sup>(a)</sup>				$7.3 \cdot 10^{-4}$			2.7	[14]
Ta <sup>(a)</sup>				$10^{-5}$			4.3	[14]
Tb <sup>(a)</sup>				$2.3 \cdot 10^{-4}$			3	[14]
Ti				$6 \cdot 10^{-6}$			4.33	[13]
Ti <sup>(b)</sup>				$3.3 \cdot 10^{-4}$				[15]
V <sup>(b), (g)</sup>				$10^{-5}$				[15]
W (111) <sup>(e)</sup>						$2 \cdot 10^{-5}$	4.5	[23]
WK <sup>+</sup> <sup>(b), (f)</sup>					$1.2 \cdot 10^{-5}$		2.8	[12]
Y				$5 \cdot 10^{-4}$			3.1	[14]
Y				$2.7 \cdot 10^{-6}$	$1.1 \cdot 10^{-6}$		3.1	[12]
Y <sup>(b)</sup>				$1.8 \cdot 10^{-4}$			3.1	[12]
Y <sup>(a)</sup>				$5 \cdot 10^{-4}$			3.1	[14]
Zn <sup>(a)</sup>				$1.4 \cdot 10^{-5}$			4.3	[14]
Zr <sup>(a)</sup>				$10^{-5}$			4.1	[14]
Zr <sup>(b)</sup>				$2.9 \cdot 10^{-4}$				[15]

$\Phi_s$  = work function from [11].

(a) = Surface preparation and activation under vacuum, from [14].

(b) = Cleaning by argon ion bombardment

(d) = ATF (BNL) measurements at 70 MV/m without surface treatment

(e) = Photoemission assisted by high electric field,  $E = 3$  GV/m

(f) = Potassium ions implanted in tungsten substrate (150 keV implantation energy, with an ion flux density of  $1.3 \times 10^{17}$  ions/cm<sup>2</sup> at the surface)

(g) = Annealing procedure at 250 °C

If no special in-vacuum treatment is applied to a metallic photocathode surface, the QE will be dominated by the contamination on the surface. Reaction of the cathode surface with air leads to surface chemistry (e.g., oxidation) that will increase the work function. The QE can then become much smaller than the values listed in Table 7.1. Figure 7.5 illustrates QE measurements taken in a diode-geometry gun where the cathode was illuminated with laser pulses at 266 nm. The metal samples were exposed to air for several weeks before being installed in the diode gun. Under such conditions the QE always stayed below  $10^{-4}$  and the QE values are very different from those of Table 2.3.1, pointing to the reactivity of the metal with ambient air.

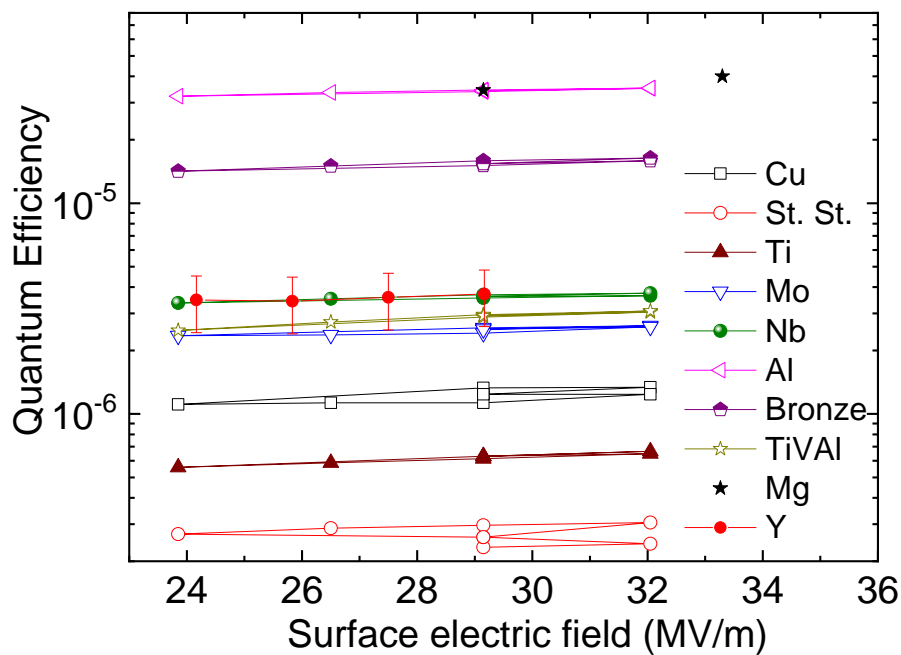


**Fig. 7.5** Quantum efficiency of various metal photocathodes measured in a diode gun (350 kV and variable gap) using 6 ps rms laser pulses at 266 nm, and 10 Hz repetition rate. Cathode samples were exposed to air without any in-vacuum cleaning treatment [13].

For an atomically clean surface, the **crystal orientation** can change the work function by several tenths of an eV, which leads to significant variations in the QE. For different crystal orientations of copper, Table 7.2 gives examples of the work-function variation; values extend from 4.48 to 4.94 eV, which is a range of 0.46 eV. The dependence of the QE on the work function is plotted in Fig. 7.6, which corresponds to (7.2) for the case of copper illuminated by 253 nm photons. Taking into account the Schottky reduction ( $\sim 0.3$  eV), the **effective work function** ranges between 4.18 eV and 4.64 eV, which corresponds to a QE variation of one order of magnitude.

**Table 7.2** Work function for four crystal orientations of copper, from [11]

Crystal Orientation	Work function (eV)
Cu Polycrystalline	4.65 +/- 0.2
Cu (100)	4.59 +/- 0.03
Cu (110)	4.48 +/- 0.03
Cu (112)	4.53 +/- 0.03
Cu (111)	4.94 +/- 0.03

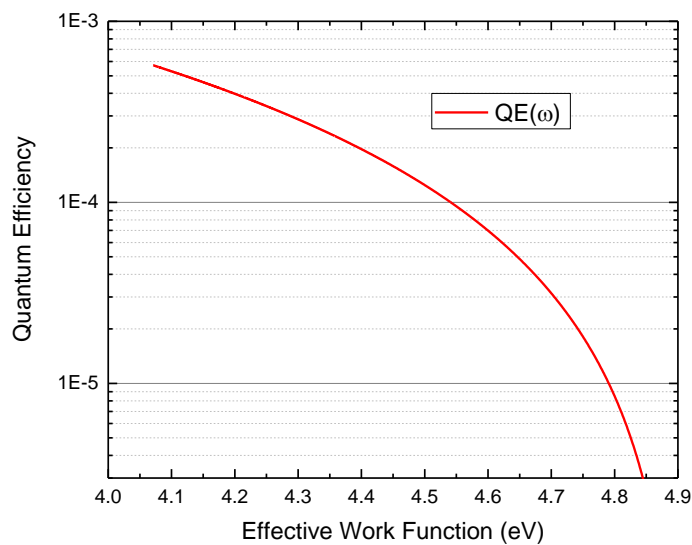


**Fig. 7.6** QE variation of copper versus work function using light at 253 nm

Figure 7.7 shows two micrographs of a **polycrystalline** copper photocathode from an RF photo-injector. The grain boundaries between different facet orientations are clearly visible and the cathode surface appears as a highly non-uniform surface. In practice, it is difficult to observe a spatial variation of QE on a polycrystalline metal surface (see, for example, the QE map of Fig. 7.11 below). But photoemission electron microscopy performed on a polycrystalline copper photocathode clearly revealed the difference of emission in the different grains [24]. A single-crystal photocathode would have the advantage of much better uniformity. Or if the typical grain size is larger than the illuminating spot size, one could also obtain **single-crystal** photoemission from a polycrystalline sample. In the RF photoinjector of the LCLS free electron laser at Stanford, a polycrystalline copper photocathode is used as an electron source. During the preparation of the cathode, the copper is fired to very high temperature (above 800 °C) such that the grain sizes grow nearly as large as the laser spot illuminating the cathode (mm). By picking a sufficiently large **grain**, photoemission is obtained from a single crystal [19].



**Fig. 7.7** Micrographs of a copper photocathode under white light illumination [17]

As illustrated in Table 7.1, the QE also decreases with increasing photon wavelength, simply because fewer electrons can be excited to sufficiently high energy to escape (see Fig. 7.1). On the other hand, electrons emitted with an energy component normal to the surface that is close above the energy level of the top of the barrier have relatively low total **kinetic energy** immediately after emission; this can be beneficial for applications where the thermal agitation of extracted electrons (intrinsic emittance) is a concern. For example, in accelerators one goal is to produce electron bunches that occupy a very small volume in phase space. This is the case when all electrons follow parallel trajectories at cathode exit without random thermal agitation.

Figure 7.8 from Vicario et al. [25] illustrates quite well the dependence of the QE on the illuminating **photon wavelength**. To fit the data they used a similar relation to (7.2) for copper.

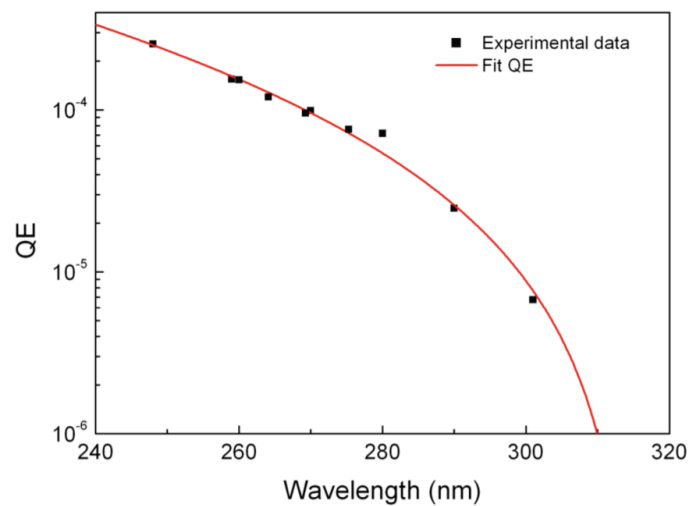


**Fig. 7.8** Quantum efficiency of a copper photocathode versus the illumination wavelength, from [25]

## 7.2.4 Limitations and potential of metallic photocathodes

### Cathode preparation: bulk material choice, polishing and cleaning techniques

As mentioned in the previous section, to obtain optimum behavior and high QE values, the preparation of the photocathode surface before and after installation in vacuum is extremely important. All metallic photocathodes produced from bulk material will have several layers of adsorbed

contaminants on the surface. These **contaminants** come from the ambient air (H<sub>2</sub>O, CO, CO<sub>2</sub>, N<sub>2</sub>, H<sub>2</sub>) and from organic chemical compounds formed during the machining and manipulation of the photocathode.

*Out-of-vacuum cleaning:*

A common cleaning technique for metals for ultra-high vacuum is hot ultrasonic washing with detergent followed by careful rinsing. **Alkaline detergent** cleaners like tetrapotassium pyrophosphate can efficiently clean metallic surfaces [26,27]. In a second step, ultrasonic cleaning with **solvents** like acetone and alcohol is a good way to remove residual grease or organic films from the surface. The photocathode should then be dried with dry air and installed under vacuum as soon as possible.

For photocathodes contaminated with an oxide layer, more aggressive techniques are needed, like mechanical polishing (discussed below) or acid **etching** (nitric, sulfuric, hydrochloric and phosphoric acid), which will remove several micrometers of material. In the case of mechanical polishing, the ultrasonic cleaning processes mentioned above are required afterwards. For both techniques, it is important to install the photocathode under vacuum as soon as possible. Indeed, after the oxide layer has been removed, the surface is very reactive and depending on the type of metal, an oxide layer can return very quickly.

*In-vacuum cleaning:*

To remove molecules adsorbed on the surface, an efficient way is to heat the photocathode under vacuum. Most of the water, hydrogen and carbon based molecules will be desorbed from the surface if the **annealing** temperature exceeds 250 °C. Figure 7.9 illustrates the effect of annealing a copper photocathode at 250 °C for 10 hours. For three different samples, the QE increased by a factor 5 to 30 after the thermal cycle [31]. Such an annealing procedure ensures an initial QE of  $\sim 10^{-4}$ , which is close to the theoretical expectation for polycrystalline copper [17].

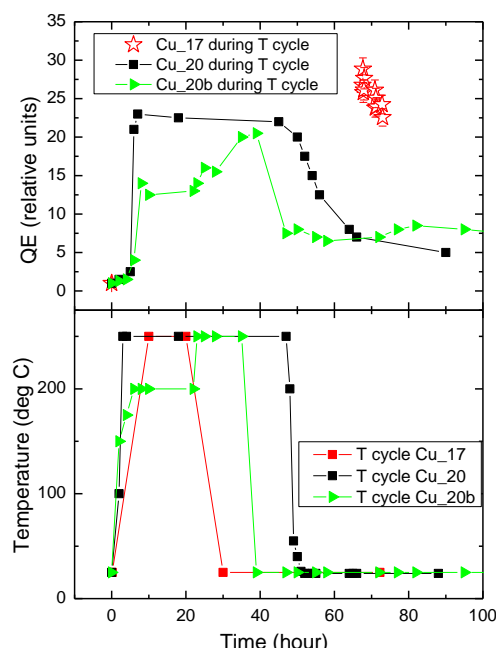


**Fig. 7.9** Effect of annealing a copper photocathode: QE (top) and temperature cycle (bottom) versus time for three samples [28]

Once the photocathode surface has been cleaned under vacuum, the only contamination which would appear again must come from the residual gas present in the vacuum chamber, such as H<sub>2</sub>, CH<sub>4</sub>, H<sub>2</sub>O, CO, O<sub>2</sub>, N<sub>2</sub>, Ar, and CO<sub>2</sub>. Assuming all the gas atoms and molecules stick to the surface, it takes only one hour to cover the surface with one monolayer at a pressure of 10<sup>-9</sup> Torr (about 10<sup>-9</sup> hPa or 10<sup>-7</sup> Pa) [29]. Luckily, the **sticking coefficient** of residual gasses such as CO and H<sub>2</sub>O is much smaller than unity and the partial pressures of these gas species can be very low. But it explains why the QE of a photocathode can degrade over time by a large amount, as in Fig. 7.19 below. Under some conditions the illuminating light can help to clean the surface, but under other conditions the light can crack the molecules leaving highly reactive chemicals that strongly adhere to the surface as illustrated by the QE hole in Fig. 7.1, located exactly at the position of the laser. In any case, a regular annealing procedure after some duration of operation will desorb most of the accumulated contaminants and restore the QE to its initial value. Another important mechanism responsible for QE variation is **ion back bombardment**. Residual gas atoms and molecules can be ionized by photoelectrons near the photocathode surface. These ions will be accelerated towards the photocathode, where they can be implanted into the material, thereby altering energy levels or reducing the electron diffusion length, or sputtering away chemicals applied to the surface that reduce the work function. This mechanism can be a major issue for DC high-voltage photoguns (see Section 4.3.3).

Several other techniques exist to clean metallic photocathodes in vacuum. The so-called **laser cleaning** technique relies on a laser beam focused close to the ablation threshold, and then scanned across the cathode surface [20]. In order to avoid the creation of large craters on the surface, a careful monitoring of the vacuum pressure during laser cleaning is required [30]. **Ozone cleaning** can also successfully desorb molecules from metallic surfaces [31]. In general, the final QE of a clean metal surface is independent of the method used to achieve the surface. Figure 7.10 shows the QE of a LCLS copper cathode prepared via laser cleaning with a 266 nm laser (~30 ps pulse duration) with an energy density of 1 mJ/mm<sup>2</sup> compared to that of a second cathode cleaned via Hydrogen ion cleaning [9]. The initial (uncleaned QE), and the three-step model theory prediction based on (7.2) are also shown.

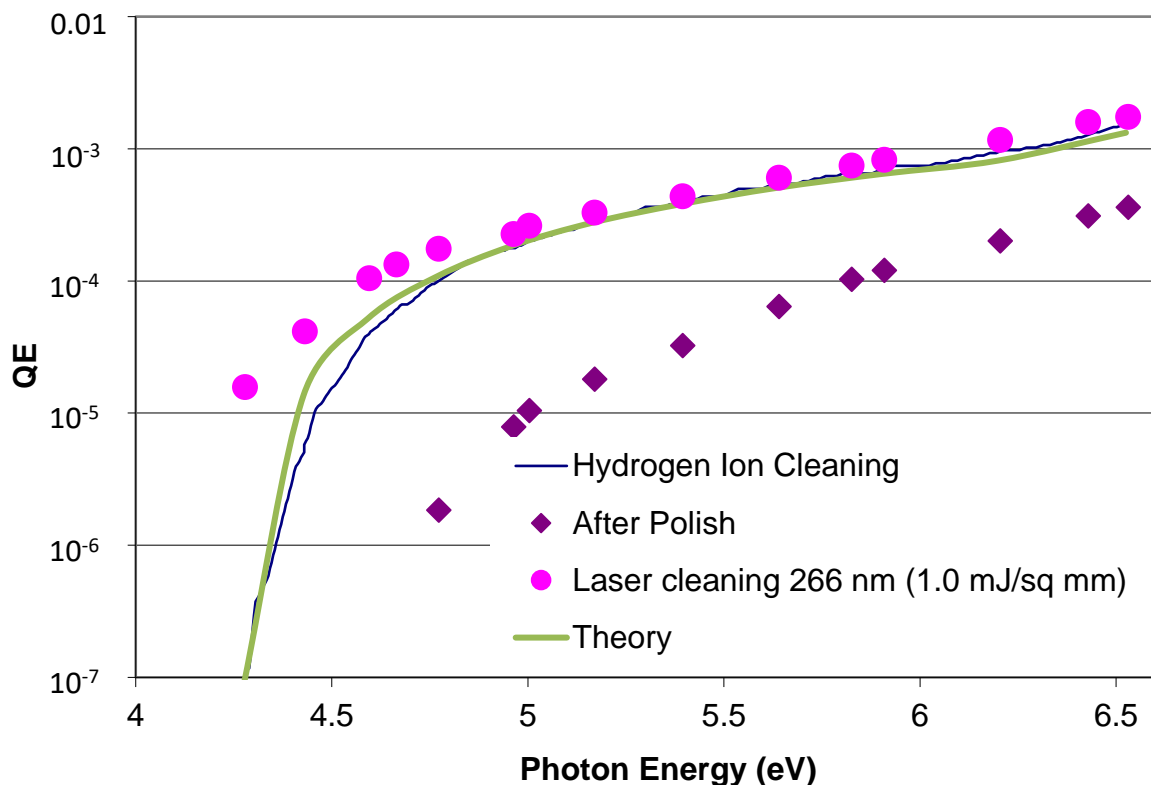


**Fig. 7.10** Comparison of three-step model theory with LCLS Cu cathodes cleaned via laser cleaning and hydrogen-ion cleaning. (Color Figure)

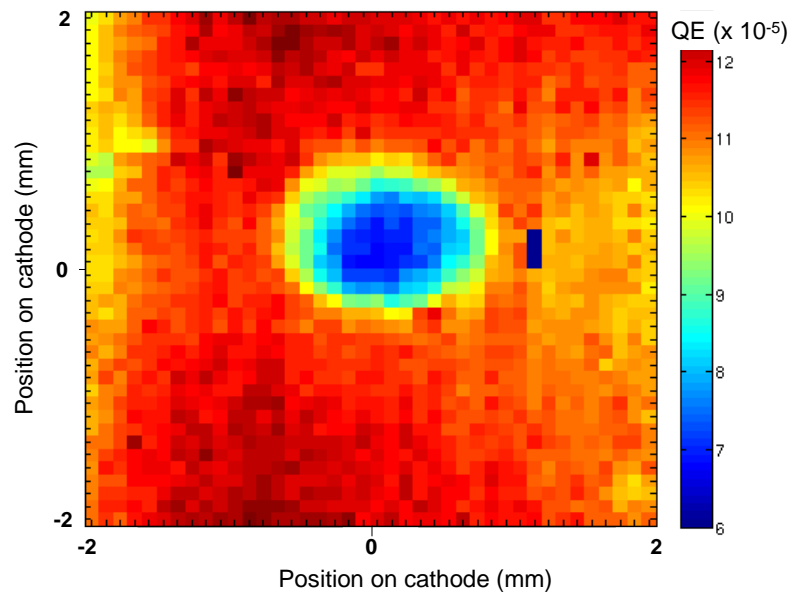


**Fig. 7.11** QE map revealing the effect of laser illumination on QE degradation. Long term illumination has the effect of cracking organic molecules which then bind to the surface (source: [28]) (Color Figure)

Figure 7.11 is a **QE map** of a copper photocathode that was used in the electron gun of an accelerator. The QE map was obtained by focusing a UV laser to a small spot (below 100  $\mu\text{m}$ ) and by scanning this spot over the full cathode surface. One can clearly distinguish a round area where the QE is reduced. This area corresponds to the region which was exposed to the full laser beam during normal operation of the electron gun. Long UV laser exposure seems to induce surface chemistry which then lowers the QE. Some labs use laser ablation to clean the surface and retrieve the original QE of the bulk photocathode material. However, such an ablation process is delicate if one wants to preserve the highly polished surface [32].

In addition to the contaminants coming from the residual gas, the photocathode material itself can contain **impurities**. Metallic cathodes made of bulk materials can reach purity levels above 99.995 %, with impurities like  $\text{O}_2$ , C, and P present within the material at a level of less than 10 ppm [33]. Metals also contain inclusions, or bubbles, which can degas once in vacuum. Metals that are forged or produced by hot isostatic pressure (HIP) methods are better for photocathode applications because they have larger grain sizes, and therefore fewer inclusions and defects compared to cast metals.

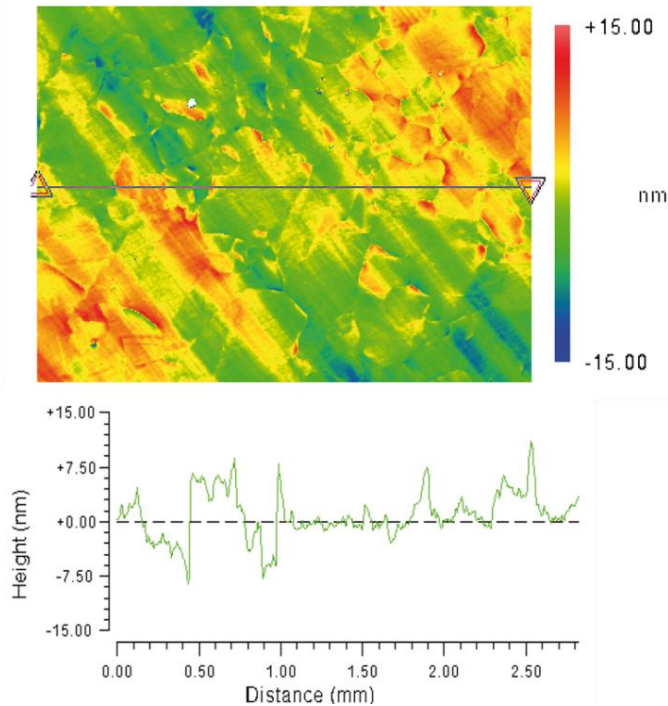


**Fig. 7.12** Top: Surface profilometry of a diamond turned copper sample 2.7 mm by 1.5 mm (forged copper). Bottom: Transverse profile along the line shown in the top figure; grain size: 300  $\mu\text{m}$ ; roughness ( $R_a$ )  $\sim$ 3 nm; height (peak-to-valley)  $\sim$  30 nm (source: [17]) (Color figure)

Metallic photocathodes made of bulk material, in contrast to those produced by thin film deposition, need to be polished. **Roughness** of the photocathode surface must be controlled since it affects the quality of the emitted beam. In accelerator photoinjectors the cathode surface roughness must be small to withstand high electric field and also to avoid beam emittance increase [34], [35]. Diamond turning of the surface using “state of the art” ultra-precision tooling provides surfaces with average roughness ( $R_a$ ) less than 5 nm. Figure 7.12 represents an interferometer micrograph of a copper surface which was diamond turned. The measured roughness was about 3 nm with peak-to-valley maxima up to 30 nm. The parallel diagonal lines seen in the background are from the machining tool. Diamond turning leaves large scale surface variations, or waviness, but still provides a better surface than manual hand polishing with diamond paste. Indeed, abrasive **polishing** with diamond grit has the drawback of leaving small inclusions in the metal, especially for soft metals like copper. The grain boundaries are also visible in Fig. 7.12 and have a typical size of a few hundred micrometers. Figure 7.13 shows a 5 by 5  $\mu\text{m}$  region of an aluminum sample which was also diamond turned. The average roughness of this sample is about 1.3 nm, but the atomic force microscope reveals some local tips as large as 37 nm. Such tips can enhance the local electric field, lowering the effective work function, and introducing non-uniformity into the distribution (across the surface) of the local photoemission current density. These emission non-uniformities can be revealed by electron-emission-imaging of the cathode surface, that is to say, in a QE map.

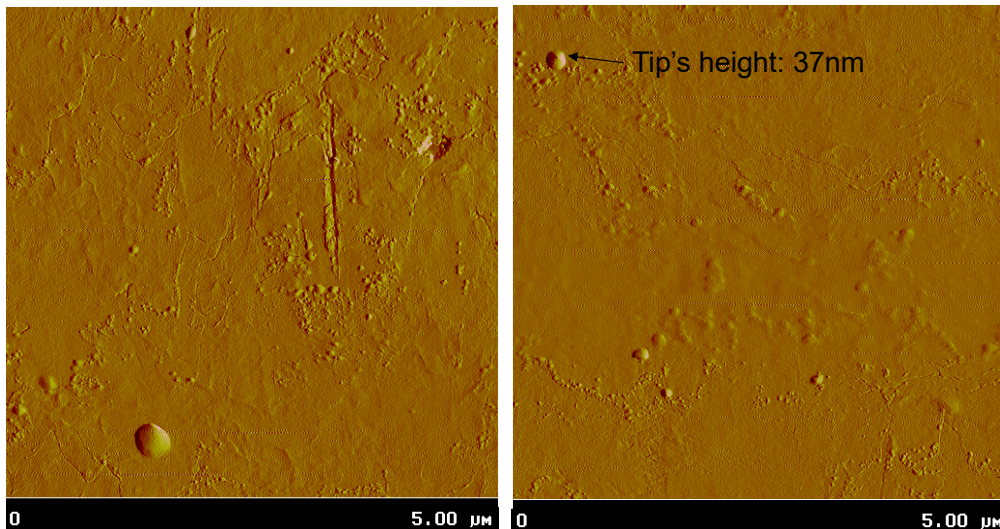


**Fig. 7.13** Atomic force microscope picture of diamond turned aluminum samples. The rms roughness is equal to 1.2 nm for this sample despite some local tips as high as 37 nm

Metal photocathodes can also be produced by growing thin films on a substrate. Pulsed laser depositions of thin films of magnesium and yttrium have been deposited onto a copper substrate [36]; these exhibited QE values similar to a bulk cathode. However, the uniformity and roughness of the obtained films remains difficult to control. **Magnetron sputtering** of Cu and Nb thin films deposited onto a Si substrate have exhibited QE values similar to those obtained with bulk materials [18].

### Incident photons

The QE performance of a photocathode depends on three parameters related to the illuminating light, as presented in (7.2):

- **wavelength**, which determines the energy of the incoming photons;
- **reflectivity**, denoted by coefficient  $R$ ;
- and the electric field component of the incident electromagnetic wave, which is called here the “**optical  $E$ -field**” (this is particularly important in the case of large incident power density and associated high optical  $E$ -field).

Because the electrostatic fields discussed in earlier sections and the optical  $E$ -fields discussed in this section may act differently on matter, and may act differently in photocathode physics, it is necessary to carefully distinguish between these two types of electric field.

The dependence of the QE on incident photon energy is illustrated in Fig. 7.8 which shows QE increasing with the photon energy, because increasingly large numbers of electrons can be excited into states with total-energies sufficient to allow escape.

If the power density of the incident photon beam is sufficiently large ( $\sim 1 \text{ W/m}^2$ ), for example because the laser beam is strongly focused or when using ultra-short laser pulses, two or (more generally)  $n$

photons can be absorbed in a single process. In this way, photo-stimulated emission of electrons becomes possible for photon energies smaller than the work function. The most favored process corresponds to the lowest value of  $n$  for which  $n\hbar\omega > \Phi_{\text{eff}}$  [39]. The dependence of the extracted current density (and hence the extracted charge per pulse) on the illuminating power will deviate from a linear behavior in the case of multi-photon processes. Multi-photon photoemission can even become more efficient than single photon emission when one considers the necessary laser power needed for frequency doubling or tripling.

The QE changes with the **polarization** of the incident light: the vectorial photoelectric effect [37]. When the angle of incidence is varied, photocathode QE can vary by factors of 2 or 3 for p-polarized light, whereas QE is almost constant for s-polarized light [38]. Evidence of QE enhancement using z-polarized laser light (i.e., optical E-field in the direction of propagation) has also been demonstrated [39]. In such a scheme, it is an electrostatic field applied to the cathode that is modified by the optical E-field.

More generally, if experimental arrangements are such that there is a component of the illuminating optical  $E$ -field normal to the photocathode surface, and this field-component is strong enough to significantly lower the effective work-function, then photoemission can be enhanced by various detailed mechanisms [40]. In particular, if the optical  $E$ -field has sufficiently high magnitude, then electrons can tunnel through the rapidly oscillating surface barrier: this effect has been called "**optical field emission**", or alternatively "**tunnelling photoemission**" [40]. The effect can be illustrated by experiments in which quasi half-cycle THz pulses were used to extract charge from a cathode surface [41]. In Fig. 7.14, a THz half-cycle with sufficiently high peak  $E$ -field (hundreds of MV/m [42]) triggered optical field emission of a pulse of electrons, with total charge close to 1 pC [C. Vicario].

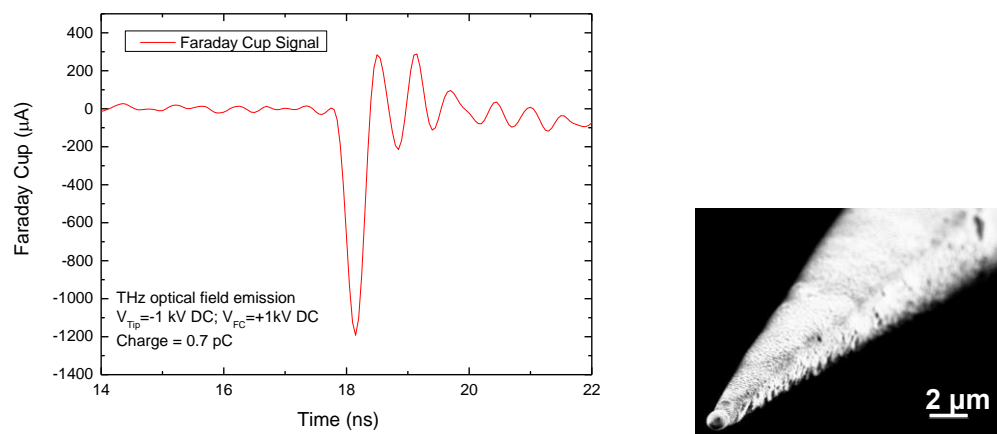


**Fig. 7.14** A quasi half-cycle THz pulse is used to trigger optical field emission from a ZrC tip. The time structure of the current pulse is limited by the scope bandwidth, but should in principle follow the THz half-cycle

### Surface Electric Field:

The local electric field component perpendicular to the cathode surface is an important parameter for the photoemission process, since (when physically negative) it lowers the PE barrier that electrons must overcome to be emitted. As noted above, this barrier lowering is known as the Schottky reduction, and is denoted by  $\Delta\Phi$ . The Schottky effect becomes significant for local fields  $F$  above a few

tens of MV/m. Such fields lower the barrier by a few tenths of an eV, the precise reduction being given by (7.1) above.

Local electric fields can be higher than the applied electric field because of enhancement effects due to the **morphological imperfections** on the surface (see Fig. 7.13). In the extreme case where the local electric field has been enhanced by geometric effects to a value of magnitude above a few GV/m, field emission can take place through the reduced PE barrier. In this case, electrons from the metal conduction band can tunnel through the barrier.

There exists an intermediate state where the barrier still prevents strong field emission but is low enough that almost all incident photons lead to electron emission, that is to say when the QE is equal to 1 or more. This was observed when sharp tips were illuminated by UV laser pulses while high voltage was applied to the tip as illustrated in Fig. 7.15 .

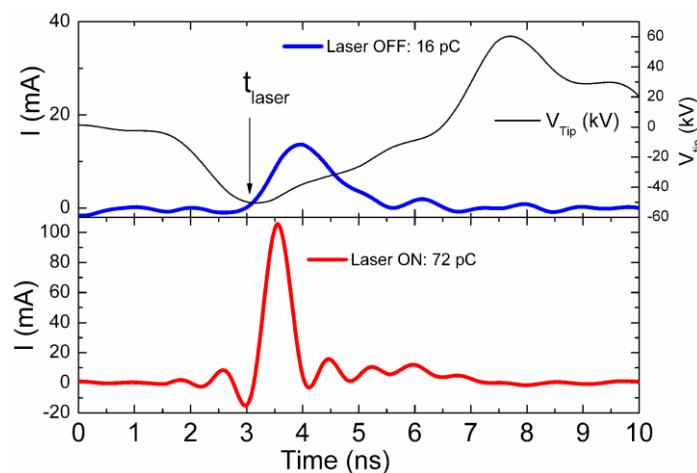


**Fig. 7.15** Top: Emitted current pulse when only a nanosecond long voltage pulse is applied (pure field emission). Bottom: Current pulse when a voltage pulse (ns) and a laser pulse (ps) are simultaneously applied. The cathode is a ZrC tip [43]

This so-called photo-assisted field emission or **photo-field emission** can be unstable since the local electric field at the apex of the tip is close to the field emission threshold, and thus close to the electric field beyond which electrical breakdown occurs in poor vacuum conditions. One way to prevent arcs is to use very short voltage pulses applied to the cathode, and short laser pulses synchronized to the field emission pulse, to trigger short pulses of photoemission. If the voltage pulses are short enough (nanosecond range), the heating effect related to the electron emission is limited and the risk of arcs is reduced. In the experiment of Fig. 7.15, voltage pulses of about 2 ns FWHM and 50 kV amplitude were applied to a ZrC tip having an apex radius of curvature of a few micrometers.

In photocathode systems, adequately high applied electric field is also desirable in order to overcome **space-charge screening** effects near the cathode. The photocathode current can be limited by poor cathode quantum efficiency, but also by an extracting electric field that is too weak. The electric field under which the electron emission starts to saturate is equal to the beam surface charge density  $\sigma$  divided by the electric constant:  $E_{SC} = \sigma / \epsilon_0$ . For example, for a short electron emission pulse of 6 ps duration, the maximum current that can be extracted from 1 mm<sup>2</sup> with a field of 50 MV/m is about 70 A.

## Superconducting photocathodes:

A special class of metallic photocathodes worthy of consideration is superconductors. The motivation for using **superconductors** as photocathodes comes from the use of superconducting RF (SRF) cavities for electron beam generation, especially for high repetition rate/CW beam operation. These cavities have nearly zero heating of the cavity walls (no RF wall losses), but they have a host of complications, including the need to keep the cavity at  $\sim 2$  K, immersed in a liquid helium bath. Putting a photocathode into an SRF injector is an engineering challenge, as the RF power can couple into and heat any normal conducting material placed in the cavity, causing the temperature to rise and the entire cavity to quench (go normal conducting). While there exist tricks to overcome this limitation, primarily through use of a quarter-wave RF choke joint and vacuum transfer systems to introduce a cathode, the simplest method of introducing a photocathode into an SRF gun is to use a material that is also superconducting.

SRF cavities are typically constructed of **niobium**, as it is an elemental superconductor available for bulk manufacture, and of all elemental superconductors it has the highest critical temperature ( $T_c$ ) and critical magnetic field ( $B_c$ ), allowing cavities constructed of niobium to support the highest electric and magnetic field gradients. Naturally, the first superconducting photocathodes were niobium [44], but niobium is a transition metal with a poor DOS for photoemission (see Fig. 7.2).

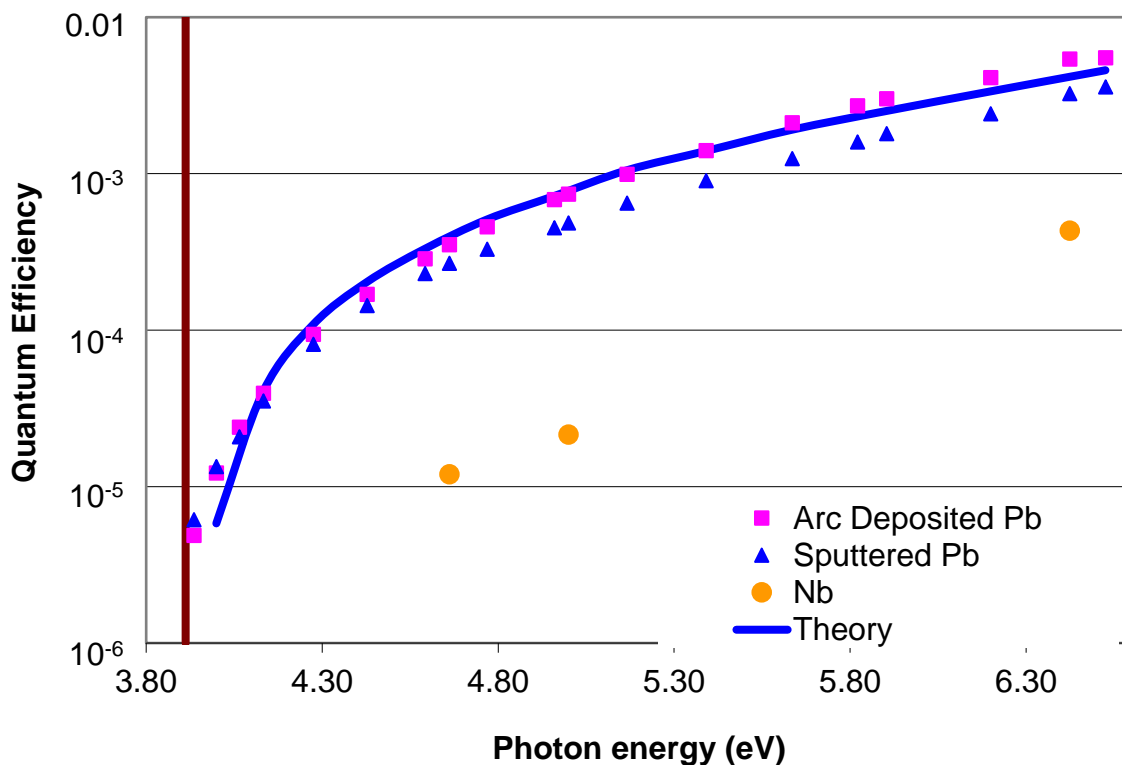


Fig. 7.16 QE vs photon energy for lead and niobium photocathodes. The vertical line represents the threshold energy for lead at zero electric field

**Lead** has also been studied as a photocathode option [45], with somewhat more success (see Fig. 7.16). Care must be taken to ensure that only lead is used in the cathode section of the injector, where the magnetic field is near zero – lead has a  $B_c$ -value one third that of niobium. However, lead is a p-band

emitter (Fig. 7.2, bottom) and has a QE roughly an order of magnitude higher than niobium in the near-threshold region. Several methods of deposition of lead onto niobium have been investigated [7,46], with vacuum arc deposition, followed by laser or plasma surface treatment, currently the preferred method.

A third superconducting photocathode option is being investigated, namely via the use of the proximity effect, by which a thin layer of a normal conducting material becomes a superconductor when it is grown on a superconducting substrate. This method is beyond the scope of this chapter.

## 7.3 Positive Electron Affinity Semiconductors

### 7.3.1 Introduction

For a semiconductor, the **electron affinity** ("EA" or  $\chi$ ) is defined as the difference ( $E_{vac} - E_{CB}$ ) between the local vacuum level ( $E_{vac}$ ) and the base ( $E_{CB}$ ) of the conduction band. This Section discusses semiconductors for which  $\chi$  is positive. Section 4 discusses semiconductors for which  $\chi$  is negative.

Alkali metals are very reactive and do not occur freely in nature. These metals have only one electron in their outer shell. Therefore, they are ready to lose that one electron in ionic bonding with other elements. **Tellurium** is a metalloid (quasi-metal) that will react with alkali metals to form a very stable compound. Amongst the alkali photocathodes,  $Cs_2Te$  is one of the most widely used compounds because of its relatively long lifetime (up to years) and because it exhibits high QE compared to other semiconductor photocathodes.

There are more than 20 different semi-conductor materials that have been developed especially for the photo-multiplier technologies, in order to cover the largest bandwidth of the spectrum (Fig. 7.17). In this Section we will focus on  $Cs_2Te$  photocathodes.

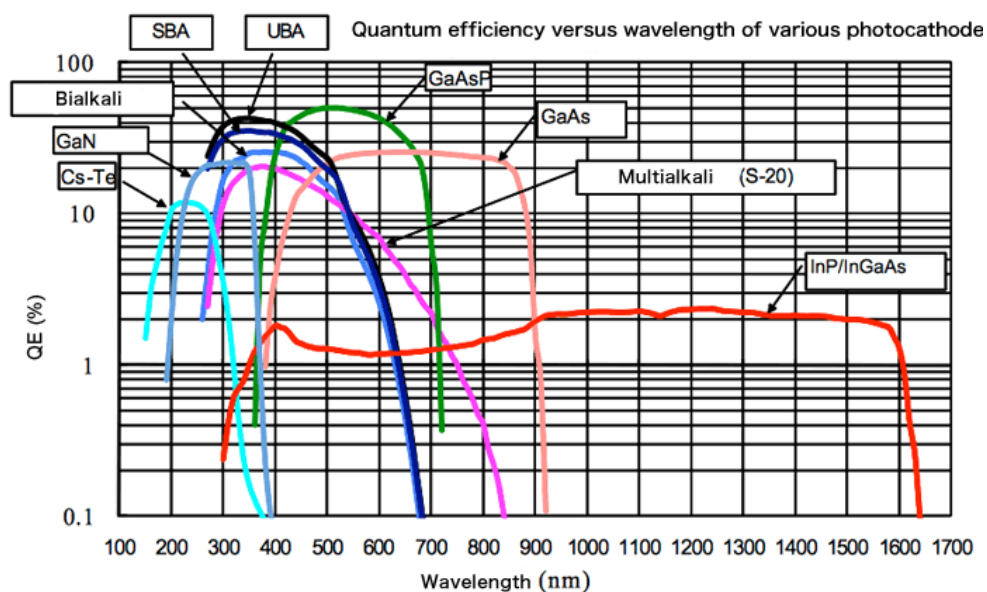


**Fig. 7.17** Overview of semiconductor photocathodes - QE versus illumination wavelength (Courtesy of Hamamatsu K. K. [47])

## 7.3.2 Preparation and performance of Cs<sub>2</sub>Te photocathodes:

### Preparation methods

Semiconductor photocathodes are produced by the deposition of thin films onto a comparatively massive substrate. For Cs<sub>2</sub>Te photocathodes, the thin films are usually obtained by **thermal evaporation** of tellurium and cesium [12]. The substrate (Al, Au, Cu, Mg, Mo, stainless steel, and others) influences the performance of the photocathode, since bulk material atoms can diffuse into the thin film. For example, Copper atoms will diffuse much deeper into tellurium than molybdenum atoms do [48]. As a consequence, better QE results and longer lifetime are obtained with molybdenum substrates.

The thickness of the evaporated Cs<sub>2</sub>Te layer can vary from a few to hundreds of nanometers. The evaporation can be done in two steps, by first evaporating a layer of Te and then a layer of Cs. The Te layer is applied first because it sticks better to the substrate than Cs. The Cs will then react with the deposited Te atoms to form various compounds (Cs<sub>2</sub>Te, Cs<sub>2</sub>Te<sub>5</sub>, Cs<sub>3</sub>Te<sub>2</sub>, Cs<sub>2</sub>Te<sub>3</sub>, Cs<sub>4</sub>Te) [49]. This successive evaporation leads to typical QE values around a few percent [50] compared to nearly 20 % when the Te and Cs are co-evaporated [51]. As the name implies, the **co-evaporation** technique consists of evaporating the Te and Cs simultaneously so that Cs<sub>2</sub>Te molecules form in the gas phase before deposition onto the cathode surface. This technique requires careful monitoring of the QE together with control of the Cs flow to reach the best stoichiometry. Figure 7.18 illustrates the evolution of the cesium source evaporation current while monitoring the photocurrent (which here corresponds to the QE) and for a quasi-constant tellurium deposition rate of 0.03 Å/s. The Cs evaporation rate is constantly adjusted to maximize the photocurrent rise. The deposition is stopped when the photocurrent starts to decrease.

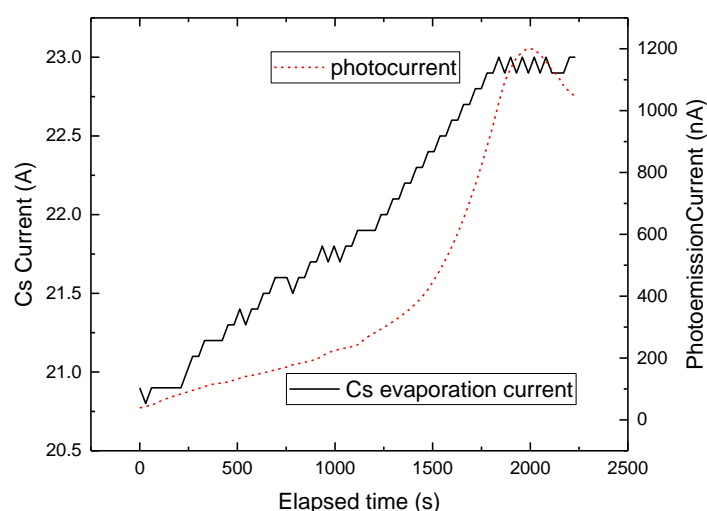


**Fig. 7.18** Evolution of the Cs evaporation current (related to the deposition rate) and collected photocurrent under constant illumination at 266 nm and while Te is deposited at 0.03 Å/s. Pressure rises to 10<sup>-8</sup> mbar during deposition

The tellurium growth process onto the substrate follows a Stransky-Krastanov [52] scheme. First Te atoms get deposited layer by layer up to a few monolayers, and then isolated islands will start to form, until the **coalescence** of these adsorbate 'islands' takes place. This results in an almost smooth surface. The Cs growing process is a pure island type of growth where some nucleation sites grow independently. The overlap of Cs on a Te layer produces a layer with a complex granularity which is a mix of the two processes described above: island and quasi-smooth surface. The resultant photocathode surface roughness is definitively larger than the roughness of the initial substrate. In the case of the co-evaporation technique, the roughness should be smaller compared to the sequential technique [53]. This can have important consequences on the beam quality (uniformity, emittance).

Due to the very high **reactivity of Cs** with oxygen [48], the newly formed thin film of Cs<sub>2</sub>Te cannot be exposed to air and has to be stored in vacuum at a pressure below 10<sup>-10</sup> mbar (10<sup>-8</sup> Pa). For this reason the semiconductor photocathode has to be transported in a vacuum suitcase and inserted into its final location via a load-lock chamber. The design of the **vacuum system** to produce and transport semiconductor photocathodes is extremely important and is usually the main cost factor of the photocathode production system.

One way to improve the uniformity of the photocathode is to heat the sample to about 100 - 150 °C during the deposition [54]. It is generally assumed that the warm sample helps to spread the islands growing on the surface. And it also helps to keep the substrate clean, particularly free of water. Finally, the warm-deposition recipe provides longer lifetime [55].

### QE values of Alkali based cathodes - Cs<sub>2</sub>Te:

The maximum QE of Cs<sub>2</sub>Te photocathodes must be discussed together with lifetime, since at very high QE values (above 10 % at 260 nm), the photocathode provides only a few hours of operation.

Table 7.3 summarizes QE values obtained with alkali metal cathodes tested under similar conditions at different laboratories. QE values as high as 20 % were reached but exhibited an exponential decay time of only a few hours. After this initial decay, the decay is still exponential but with a much longer time constant. In most cases reported, Cs<sub>2</sub>Te photocathodes could maintain QE above 1 % for at least several months, depending on the level of vacuum and the amount of charge extracted.

**Table 7.3** Overview of QE of alkali metals measured at different laboratories under slightly different conditions based on the table from [56] and updated with some recent results. [Note: 1 mbar = 100 Pa.]

Material	Substrate	QE at $\lambda$	Lifetime	Field (MV/m)	Operating vacuum (mbar)	Reference
CsI-Ge		0.73 % at 213 nm 0.13% at 266 nm	$T_{1/\tau} > 1$ year	70		[12]
		2% at 209 nm	$T_{1/\tau} > 150$ h		10 <sup>-10</sup> -10 <sup>-9</sup>	[57]
Cs <sub>3</sub> Sb	Cu	7.5% at 532 nm	> 1% over 30 h	7	10 <sup>-10</sup>	[10,51,58]
	Cu	4.9% at 532 nm	> 1% over 30 h	85	10 <sup>-10</sup>	[58]
		4 % at 527 nm	$T_{1/\tau} < 4$ h	20	10 <sup>-10</sup> -10 <sup>-9</sup>	[57]
K <sub>3</sub> Sb		1.6 % at 266 nm				[12]
		0.3 % at 541 nm				[59]
		1-3 % at 262 nm				[12]
K <sub>2</sub> CsSb		8 % at 527 nm	$T_{1/\tau} < 4$ h	20	10 <sup>-10</sup> -10 <sup>-9</sup>	[60]
		1.2 % at 541 nm	$T_{1/\tau} < 24$ h			[59]

Cs <sub>2</sub> Te	Cu - Au	16 % at 262 nm	450 h above 1.5 %	100	1-5.10 <sup>-9</sup>	[61]
	Cu -Au	2 – 8 % at 262 nm	Few weeks > 1.5 %	120	1-5.10 <sup>-9</sup>	[51]
	Cu	20 % at 266 nm	300 h above 3%	120	10 <sup>-9</sup>	[51]
	Mo	20 % at 262 nm	200 days above 4%	35 - 40	10 <sup>-10</sup>	[62]
		15.5 % at 263 nm	1 month above 1 %		5*10 <sup>-8</sup>	[63]
	Mo	16-18 % at 251 nm 8 -12 % at 263 nm	> 1% over 100 h	20 - 25	10 <sup>-10</sup>	[57]
		15- 20 % at 266 nm			10 <sup>-9</sup>	[64]
		8 – 15 % at 266 nm	> 1% over 420 days		10 <sup>-9</sup>	[65,66]

Compared to typical QE values of metal photocathodes, even a QE of 0.1 % represents a large value. If such a QE can be maintained over many months of operation, then it becomes an interesting candidate for many applications [67]. Figure 7.19 summarizes the time evolution of the QE for several copper and Cs<sub>2</sub>Te photocathode samples operated in the same RF photoinjector and under the same experimental conditions. Both photocathodes undergo QE degradation, but on average the Cs<sub>2</sub>Te photocathode has a QE one order of magnitude larger than copper for at least 100 days. For the sample Cs<sub>2</sub>Te\_17, the total amount of extracted charge was 3 mC, without major sign of degradation.

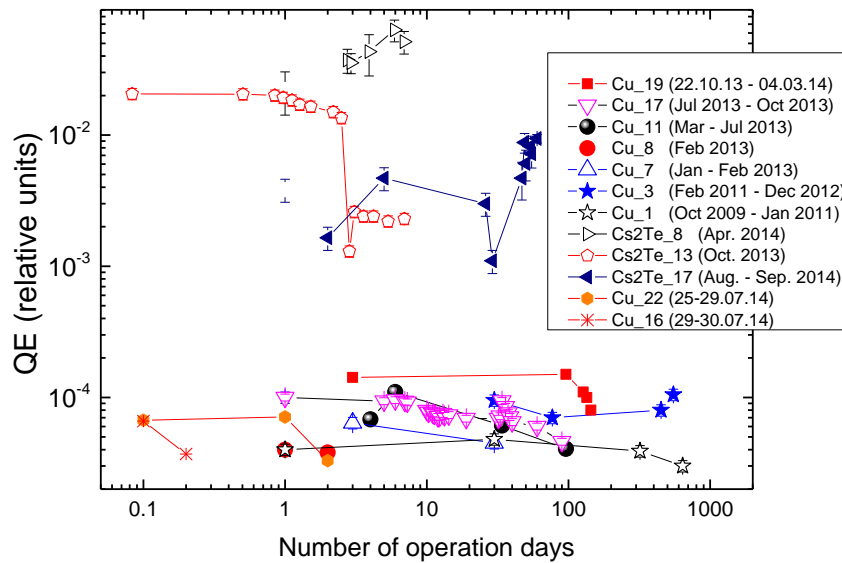


**Fig. 7.19** Evolution of QE with time for various copper and Cs<sub>2</sub>Te photocathodes operating under the same conditions: extracting field 52 MV/m, 262 nm laser pulses of 4 ps rms duration at 10 Hz repetition rate, with 10<sup>-9</sup> mbar (10<sup>-7</sup> Pa) photogun vacuum.

### 7.3.3 Sensitivity to vacuum

As mentioned above, the main drawback of semiconductor photocathodes as compared with metals is their high sensitivity to oxygen [48]. The poisoning of the photocathode surface can affect both the lifetime of the cathode and the uniformity of the photoemission. A common way to measure the emission uniformity of involves scanning a small laser spot over the entire emitting area while

recording the QE at each position, to obtain a QE map. The QE maps of Cs<sub>2</sub>Te photocathodes can illustrate **non-uniformity** as shown in Fig. 7.20. Such non-uniformities are not good for beam quality and might be a result of the deposition procedure.

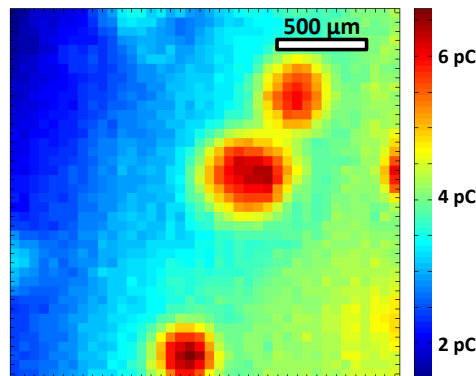


**Fig. 7.20** QE map of a Cs<sub>2</sub>Te photocathode measured inside the gun by scanning a small laser spot with constant energy.

Photocathode lifetime is always an important criterion for semiconductor photocathodes. The QE degradation comes mainly from O<sub>2</sub> and CO<sub>2</sub> [48,68]. Figure 7.21 shows the typical **lifetime** of Cs<sub>2</sub>Te photocathodes under the operating conditions of an RF photoinjector at the Free Electron Laser (FEL) FLASH in Germany. A photocathode lasts typically one to six months, depending on the operating pressure, and produces up to 10 μA continuous delivery, up to a total of 1 C in six months [69].

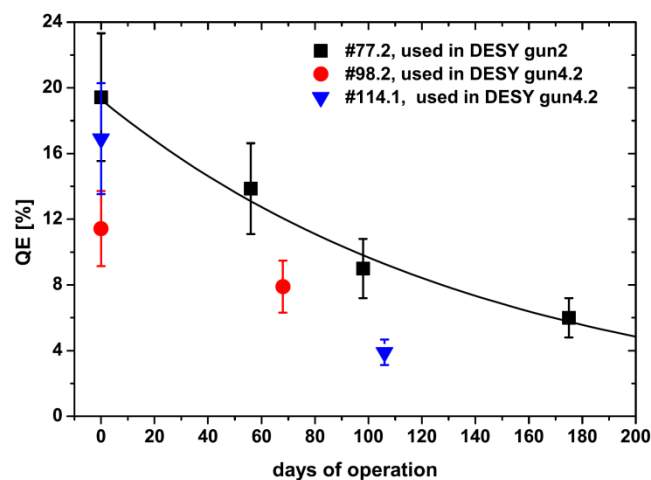


**Fig. 7.21** Typical lifetime of Cs<sub>2</sub>Te photocathodes used in an RF photoinjector: Illumination with trains of 2400 laser pulses of ps duration during an 800 μs macropulse at 10 Hz, 262 nm illumination, 40 MV/m, 700 pC/pulse (source: [62])

### 7.3.4 Alkali-Antimonide photocathodes:

Image intensifiers (for night-vision), and low-light-level detectors (photomultiplier tubes) are normally vacuum emissive devices. For such devices, the most common photocathodes come from the alkali-antimonide family. These materials typically consist of 3 alkali atoms and one antimony atom per molecule, and some photocathodes (such as the S-20) use multiple layers of differing composition. Commonly used photocathodes of this family include Cs<sub>3</sub>Sb, K<sub>2</sub>CsSb, Na<sub>2</sub>KSb, and (Cs) Na<sub>2</sub>KSb (S20),

though others are used as well. For accelerators, this class of materials holds the average-current record for both DC and RF photoinjectors [70], [71].

### Preparation methods and film properties

Several sources have been used to provide alkali materials for growth, including thermal evaporation from sealed sources, chromates, alkali azides, and pure alkali metal effusion sources. In most of these cases, antimony is provided via thermal evaporation, either from Sb pellets in a crucible or from Sb (or PtSb alloy) wire sources. Recently, sputter growth of  $C_3Sb$  and  $K_2CsSb$  has also been demonstrated [72]. Vacuum is critical in alkali antimonide growth – these materials degrade quickly in a partial pressure of water over  $10^{-8}$  Pa. However, the cathodes are relatively insensitive to most other gases – alkali antimonide cathodes are routinely operated in gas electron multiplier-based detectors at ambient pressure of Ar and  $CH_4$ .

The structure of an alkali-antimonide film is a strong function of whether the growth is sequential (Sb-K-Cs, for example), or via co-deposition/sputtering. Traditional growth has involved sequential deposition of Sb, followed by the weakly bonded alkali, followed by the strongly bonded alkali (typically Cs). This results in a good QE, but the lattice mismatch between crystalline Sb [73] and the cubic alkali antimonides results in significant roughening of the surface (up to 25 nm RMS for a 50 nm thick film [74]).

Co-evaporation of Sb and the alkalis avoids this recrystallization, and results in a far smoother film [75]. It has also been shown to dramatically improve the lifetime of cathodes for detector applications [76]. It is, however, significantly more difficult to control. These methods have resulted in surfaces with RMS roughness under 1 nm. Co-evaporation also produces superior QE performance, as shown in Fig. 7.22.

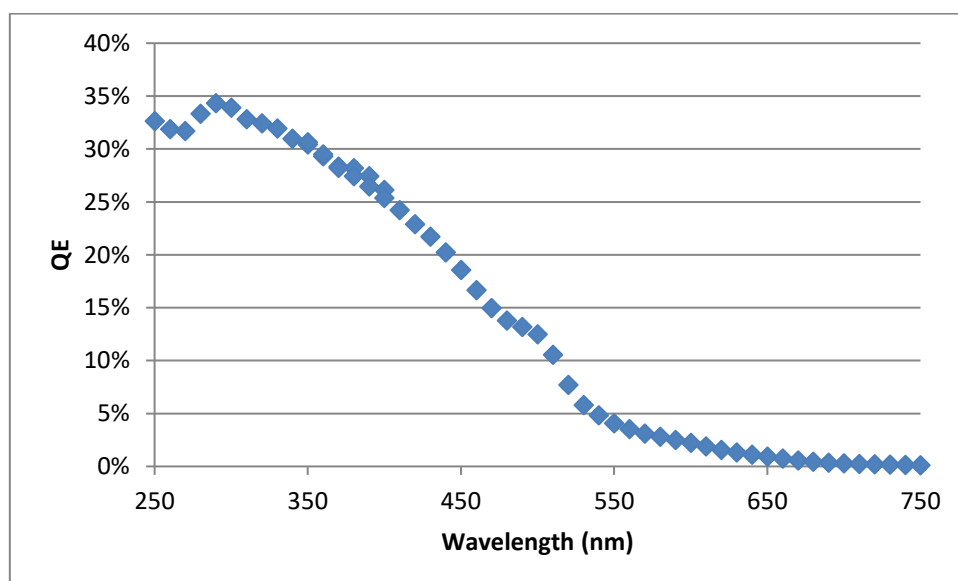


**Fig. 7.22** Spectral response of a  $K_2CsSb$  photocathode grown by ternary co-evaporation with in situ X-ray fluorescent monitoring

Sputter growth produces films that are largely amorphous but very smooth (RMS  $\sim 0.5$  nm for a 50 nm film). These films have lower QE (typically 16-20 % peak, and 4 % in the green, as compared to 35 % and 8-10 % for sequential and co-evaporated cathodes), but are easy to produce over large areas.

For many applications, the roughness of the cathode is not an important parameter, but for accelerators it has a dramatic impact on the source emittance and achievable brightness [77]. It is also important for detector applications that require high electric fields.

### *In situ* x-ray analysis during growth

Much of the recent progress in alkali antimonide growth is the result of new tools which have been developed to study thin film growth [78]. Using an x-ray beam from a synchrotron (such as the National Synchrotron Light Source II at Brookhaven National Laboratory or the Cornell High Energy Synchrotron Source at Cornell University), the material crystal structure, stoichiometry and surface roughness can be evaluated in real-time during growth, even under UHV conditions. The critical techniques used for *in situ* analysis are x-ray diffraction XRD for determining crystal structure evolution, x-ray fluorescence for measuring stoichiometric evolution and x-ray reflectivity for measurement of surface roughness. Fig. 7.23 shows the XRD evolution of a cathode grown through traditional sequential deposition, along with the thickness (monitored via quartz crystal monitor) and the QE.

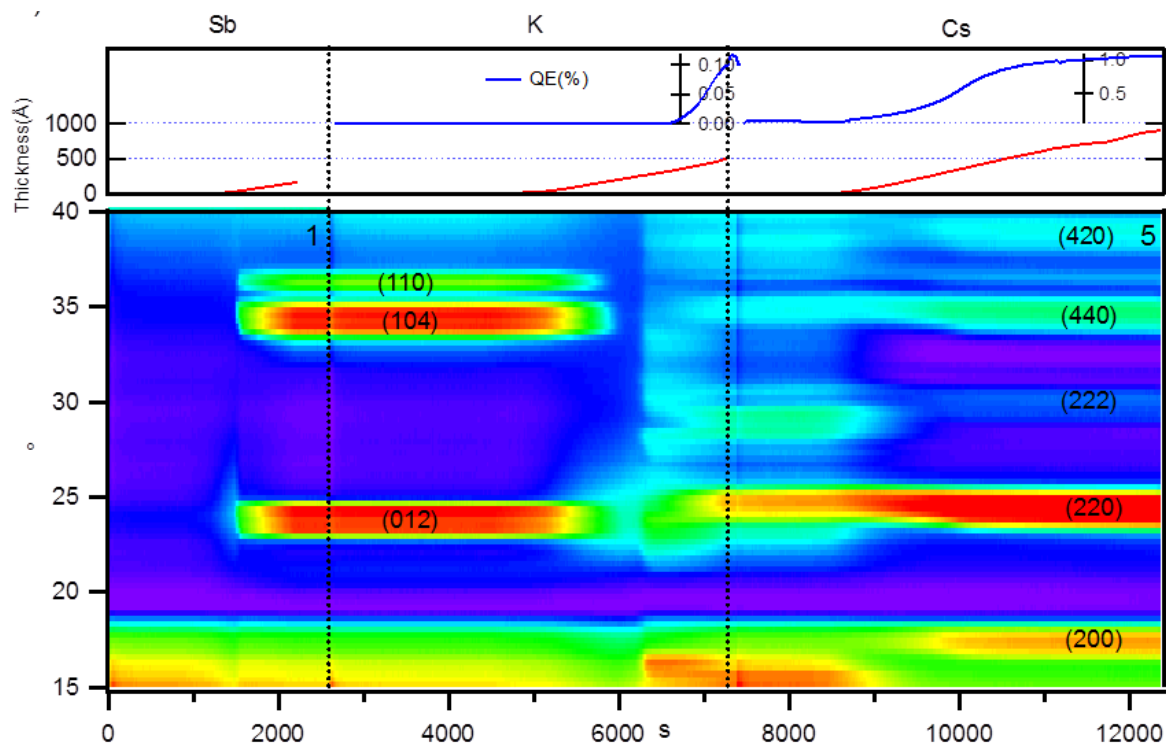


**Fig. 7.23** XRD evolution of sequential  $K_2CsSb$  growth, showing the crystallization of the antimony film at 4 nm thick. This is followed by potassium deposition which causes the film to go amorphous at  $\sim 6000$  s into the deposition. When the film recrystallizes into potassium antimonide, the QE (top plot) begins to rise

## 7.4 NEA Semiconductors: GaAs based photocathodes for polarized electron beams

### 7.4.1 Overview of GaAs photocathodes

Polarized electron beams play a critical role in nuclear and high energy physics research, including parity-violating electron scattering experiments and the measurement of nucleon spin structure functions [79], [80]. As recently demonstrated, spin-polarized electron beams can also be used for magnetization-sensitive imaging [81]. The first **polarized electron source** for an accelerator, based on photo-ionization of state-selected  ${}^6\text{Li}$  atoms, was developed at Yale University in the early 1970s, for use at the Stanford Linear Accelerator (SLAC) [82]. Later, a polarized electron source based on the Fano effect in Rb was developed for the Bonn synchrotron [83]. Other polarized sources were developed or proposed during the 1970s, including an improved version of the Li photo-ionization source [84], a source based on the chemi-ionization of metastable He atoms [85], and sources using the Fano effect in Cs [86]. None of these latter sources were ever developed to the point of being operational at accelerators. Following the 1974 demonstration [91] of polarized photoemission from GaAs at low voltage, a high-voltage source was constructed at SLAC [87]. This was used to conduct the seminal parity-violation experiment E122 [88] that verified predictions by Wienberg and Salam, and thereby helped to establish the Standard Model of electro-weak physics. Shortly thereafter, polarized electron sources using **GaAs photocathodes** with an NEA surface condition were constructed at MIT-Bates [89], NIKHEV [90], the Mainz Microtron [91], Bonn-ELSA [92], Nagoya University [93] and CEBAF-Jefferson Lab [94].

Photocathode QE and electron spin polarization (ESP) are important characteristics of GaAs photocathodes. For decades, photocathode experts have worked to increase these quantities. The QE of GaAs photocathodes is affected by many factors, including cathode material quality, the wavelength of the incident light, the thickness of the photocathode, dopant density, the photocathode temperature, surface contamination, the negative-electron-affinity condition on the photocathode surface, the power density of the laser light, the bias voltage (i.e., Schottky effect), and the vacuum pressure under which photo-extracted beam is produced. These factors also affect ESP via spin relaxation/depolarization mechanisms that influence conduction-band electrons as they migrate toward the photocathode surface and are then emitted into vacuum. This section provides an overview of polarization and ion bombardment effects, which are the chief lifetime-limiting factors of a NEA GaAs photocathode inside a high voltage photogun.

GaAs is a direct-transition III-V semiconductor with zincblende crystal structure. It can absorb laser light across the broad visible spectrum, but only illumination with near-IR wavelengths provides polarized photoemission. This can be understood by looking at detailed [95] and simplified representations [96] of the energy level diagrams of GaAs (Fig. 7.24). Electron spin-orbit coupling splits the  $P_{1/2}$  and  $P_{3/2}$  energy levels of the valence band into two states separated by 0.33 eV, which is large enough to avoid optical pumping from the lower energy  $P_{1/2}$  state. Polarized photoemission takes advantage of the quantum-mechanical selection rules, noting that for circularly polarized laser light, conservation of angular momentum requires an electron's spin-angular momentum quantum number to change by one unit,  $\Delta m_j = \pm 1$ . Furthermore, some transitions are more favorable than others as indicated by the transition probabilities shown in Fig. 7.24 (right). By using circularly polarized laser light with near-bandgap energy, the conduction band can be preferentially populated with a particular

spin state. Polarization is defined as  $P = \frac{N_{\uparrow} - N_{\downarrow}}{N_{\uparrow} + N_{\downarrow}}$  where  $N$  refers to the number of electrons in the conduction band of each spin state, “up” or “down”. For bulk GaAs, the theoretical maximum polarization is 50%, corresponding to three electrons of the desired spin state for every one electron with opposite spin.

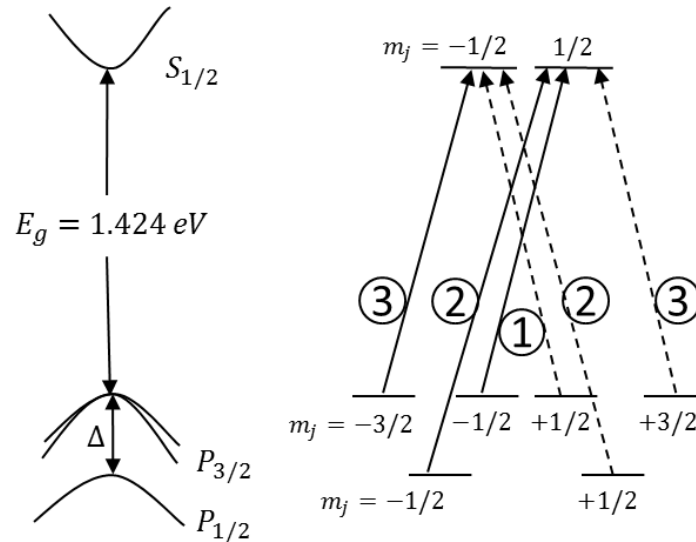


**Fig. 7.24** (Left) Energy level diagram of GaAs at the center of the Brillouin zone: a “close-up” view near the valance band maxima/conduction band minima, and (right) simplified view showing the optical transitions between sublevels for right circularly polarized light (solid lines) and left circularly polarized light (dashed lines), with relative transition strengths given by circled numbers

As discussed previously for other photocathodes, the emission of electrons from GaAs can be described as a **three-step process** [3] involving absorption of light, diffusion of electrons to the surface of the photocathode, and emission of the electrons into the gun vacuum chamber. However, it is worth mentioning two aspects of efficient photoemission that are unique to GaAs. Namely, efficient photoemission from GaAs requires that the material be p-doped [97], which serves to lower the Fermi level (relative to the band edges) throughout the material. The p-doping—when acting together with the negative applied external field and (in some cases) other effects—also serves to induce band-bending and lower the conduction band at the surface of the photocathode; this in turn reduces the **electron affinity** (to the new value  $EA_{\text{eff}}$  in Fig. 7.25b). Secondly, no significant photoemission is obtained until the potential barrier is reduced further and this is accomplished by adding about a mono-layer of cesium and oxidant (Fig. 7.25c). The process of adding cesium and oxidant to the photocathode surface to create the desired NEA condition is called “activation”.

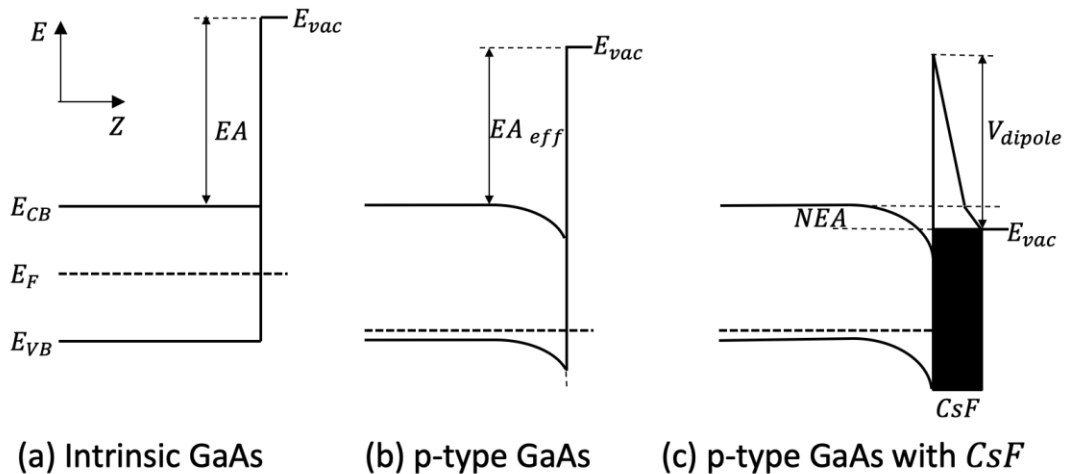


**Fig. 7.25** Energy level diagrams describing the formation of the negative electron affinity (NEA) condition on GaAs.  $E_{CB}$ ,  $E_F$ ,  $E_{VB}$ , and  $E_{vac}$  describe the conduction band base energy, the Fermi level, the valence band maximum energy and the local vacuum energy level, respectively.  $EA$  and  $EA_{eff}$  refer to the local electron affinity, and the latter determines the so-called "surface work function"  $\phi_s$ , defined by  $\phi_s = E_{vac} - E_F$ .  $V_{dipole}$  is the further decrease in effective electron affinity caused by the CsF activation layer. The diagrams show: (a) intrinsic GaAs; (b) how p-type dopant lowers the Fermi level which—together with the negative applied external field and (in some cases) other effects—leads to downwards band bending at the surface; and (c) how adding a CsF layer lowers the surface potential-energy barrier and leads to further band bending, to a lower surface work function, and to the desired NEA condition.

At room temperature, highly doped bulk GaAs photocathodes typically provide ESP of the order  $\sim 30\%$ , a value considerably less than the theoretical maximum value of  $50\%$ . The investigation of **spin relaxation** and depolarization has a long history dating back to the 1950s, [98] [99]. The literature describes two main spin relaxation mechanisms for p-type III-V semiconductors: 1) the lack of inversion symmetry in III-V semiconductor leads to a spin splitting of the conduction band, called the D'yakonov-Perel (DP) mechanism [100], and 2) the exchange interaction between electrons and holes, called the Bir-Aronov-Pikus (BAP) mechanism [101]. As described below, for p-type GaAs, the BAP mechanism dominates with the DP mechanism playing a role at high temperature and low dopant concentration [102] [103]. There are other depolarization processes, but these are typically considered to have little consequence and are frequently ignored. These include the Elliot-Yafet (EY) mechanism [104], in which the spin-orbit interaction generates non-pure spin states in the conduction band, and radiation trapping, in which ESP is diluted by supplemental photoemission that results from the absorption of linearly polarized recombination light. There is a wealth of literature describing polarization studies using bulk GaAs, as a function of temperature [105]-[106], dopant concentration [97]-[99] electron (and hole) density [107], and thickness of the photocathode [98]. In sections below, recent measurements are summarized describing ESP sensitivity to sample temperature and Zn dopant density, which have a significant impact on ESP. In general, ESP can be increased at the expense of QE.

## 7.4.2 Theory: Spin relaxation mechanisms

Electrons in the conduction band will arrive at an equilibrium polarization when the photocathode reaches a steady-state condition defined as,  $dP/dt = P_0/\tau - P/\tau - P/\tau_s = 0$ . The term  $P_0/\tau$  is the rate of polarization creation using circularly polarized light,  $P/\tau$  describes polarization loss due to electron recombination to the valence band, and  $P/\tau_s$  is the rate at which polarization disappears due to spin relaxation effects. So the equilibrium polarization is given by [105];

$$P = P_0 \frac{1}{1 + \frac{\tau}{\tau_s}} \quad (7.3)$$

where  $P_0$  is the initial polarization determined by the quantum-mechanical selection rules (as mentioned above,  $P_0 = 50\%$  for bulk GaAs),  $\tau$  and  $\tau_s$  describe the electron lifetime and spin relaxation time for electrons at the bottom of the conduction band, respectively. The electron lifetime  $\tau$  of GaAs is of the order  $10^{-9}$  to  $10^{-10}$  s, with the exact value dependent on the temperature and doping concentration of the sample. The cumulative **spin relaxation time** is composed of individual spin relaxation mechanisms given by,  $1/\tau_s = 1/\tau_s^{DP} + 1/\tau_s^{BAP} + 1/\tau_s^{EY} + 1/\tau_s^{rad}$ , where the superscripts represent the different spin relaxation mechanisms mentioned above. For p-type GaAs, the terms related to the EY mechanism and radiation trapping can be neglected.

The lack of inversion symmetry in GaAs is due to the presence of two distinct atoms in the Bravais lattice, such that the momentum states of the spin-up and spin-down electrons are not degenerate:  $E_{k\uparrow} \neq E_{k\downarrow}$ . The resulting energy difference plays the role of an effective magnetic field and results in spin precession during the time between collisions, which contributes to spin relaxation because the magnitude and direction of  $\vec{k}$  changes in an uncontrolled way. This is the so called DP mechanism, and the **spin relaxation rate** is given by [100,108] :

$$\frac{1}{\tau_s^{DP}} = Q\tau_p\alpha_0^2 \frac{(k_B T)^3}{\hbar^2 E_g}, \quad (7.4)$$

where  $Q$  is a dimensionless factor and ranges from 0.8 to 2.7 depending on the dominant momentum scattering mechanism,  $\tau_p$  is the momentum relaxation time,  $\alpha_0$  is a dimensionless parameter specifying the strength of the spin-orbit interaction ( $\alpha_0 = 4\Delta m_e/m_{ev} \left( (E_g + \Delta)(3E_g + 2\Delta) \right)^{\frac{1}{2}}$ , where  $m_e$  is the effective mass of the electron,  $m_{ev}$  is a constant close in magnitude to the mass of the free electron) and  $E_g$  is the bandgap of GaAs. The temperature dependence of the spin relaxation rate is  $1/\tau_s^{DP} \sim T^3 \tau_p \sim T^{9/2}$  [109] .

In p-type GaAs, spin relaxation can result from the spin exchange interaction between electrons and holes. This is the so-called BAP mechanism, and the spin relaxation rate is given by two terms [101]. In the case of exchange with nondegenerate holes:

$$\frac{1}{\tau_s^{BAP}} = \frac{2}{\tau_0} N_A a_B^3 \frac{v_k}{v_B} \left[ \frac{N\hbar}{N_A} |\psi(0)|^4 + \frac{5}{3} \frac{N_A - N\hbar}{N_A} \right], \quad (7.5)$$

where  $\tau_0$  is an exchange splitting parameter given by  $1/\tau_0 = (3\pi/64) \Delta_{ex}^2 / \hbar E_B$  (where  $\Delta_{ex}$  is the exchange splitting of the excitonic ground state and  $E_B = \hbar^2 / 2m_e a_B^2$  is the Bohr exciton energy),

$a_B = \hbar^2 \epsilon / e^2 m_e$  is the Bohr exciton radius,  $v_k$  is the electron velocity,  $v_B = \hbar / m_e a_B$  is the Bohr exciton velocity,  $N_h$  is the density of free holes, and  $|\psi(0)|^2$  is Sommerfeld's factor).

In the case of exchange with degenerate holes and when the electron velocity  $v_k$  is greater than the Fermi velocity of the holes, the spin relaxation rate is given by [108]:

$$\frac{1}{\tau_s^{BAP}} = \frac{3}{\tau_0} N_h a_B^3 \frac{v_k k_B T}{v_B E_{fh}}, \quad (7.6)$$

where  $E_{fh}$  is the hole energy at the Fermi level [109]-[108]. If the electrons are thermalized,  $v_k$  needs to be replaced by the thermal velocity  $v_e = (3k_B T / m_e)^{1/2}$ .

The temperature dependence of  $\tau_s^{BAP}$  is dominated by the temperature of  $|\psi(0)|^2$  as well as by the density of free holes  $N_h$ . The dependence on the acceptor density is essentially  $1/\tau_s^{BAP} \sim N_A$  for nondegenerate holes from (7.5), and  $1/\tau_s^{BAP} \sim N_A^{1/3}$  for degenerate holes from Eq. (7.6). In between these regimes,  $1/\tau_s^{BAP}$  is only weakly dependent on  $N_A$ .

The formulas cited above were used to calculate the **spin relaxation rate** as a function of temperature for bulk GaAs with dopant concentrations  $1 \times 10^{19} \text{ cm}^{-3}$  and  $5 \times 10^{17} \text{ cm}^{-3}$ , as shown in Fig. 7.26. The BAP mechanism clearly dominates over the DP mechanism, which contributes appreciably only at higher temperature. The clear message from this plot is that low spin relaxation rates—and therefore higher ESP—will be obtained at lower dopant densities and temperatures.

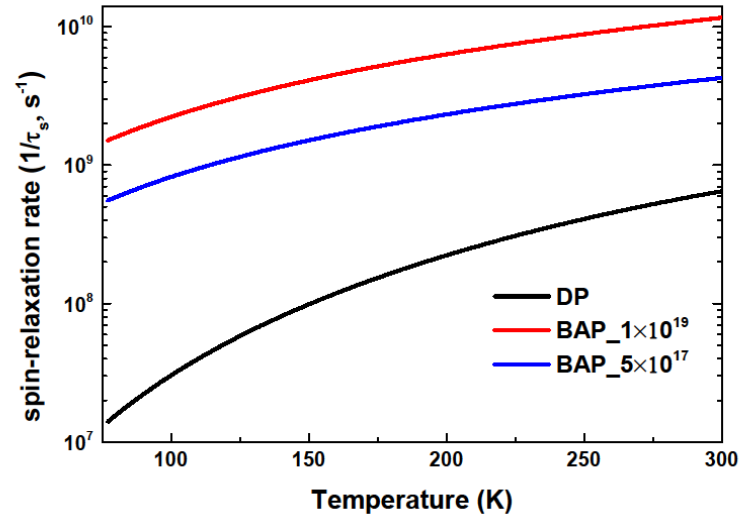


**Fig. 7.26** Temperature dependence of the spin relaxation rate for the DP mechanism, BAP mechanism and the total value in bulk GaAs

### 7.4.3 Recent Measurements with GaAs NEA Photocathodes

#### Bulk GaAs Polarization Study - Temperature and Dopant Dependence

In a recent work [110], three bulk GaAs photocathodes, each with 100 surface cleave plane but with dopant densities spanning roughly 1.5 orders of magnitude, were activated at room temperature and evaluated using a retarding field Mott-polarimeter apparatus [111]. Photocathode QE and ESP were

measured as a function of illumination wavelength, first at room temperature and then with a sample holder filled with dry ice (195 K) and LN<sub>2</sub> (77 K). The QE and ESP spectral scans presented in Fig. 7.27 exhibit the typical shape for bulk GaAs, namely that ESP increases while QE decreases as the energy (wavelength) of the illumination light is decreased (increased), with the highest polarization obtained when the energy of the light is equal to the semiconductor bandgap ensuring that only electrons from the P<sub>3/2</sub> ground state are excited to the conduction band. More interesting is the effect of **dopant density** on QE and ESP. Higher dopant concentrations serve to increase band bending, which lowers the surface work function, which increases the **electron escape probability** and leads to higher QE, however at the expense of polarization. For the commonly used dopant density of 10<sup>19</sup> cm<sup>-3</sup>, photocathode QE at room temperature reached ~ 6.9 %, but provided a maximum ESP of only ~ 30 %. Polarization increased to ~ 41 % for the low-doped sample, but provided QE of only ~ 1.5 %. This behavior is consistent with the predictions of the BAP mechanism that describes the spin relaxation rate as proportional to the dopant concentration. Higher dopant concentration leads to greater spin relaxation rate, and thus lower ESP.

Cooling the samples to 77 K modifies the crystal lattice structure and shifts the bandgap energy [112]. This bandgap shift means that peak polarization occurs at higher photon energies. The bandgap energy for GaAs can be calculated using the relation

$$E_g(T)/\text{eV} = 1.519 - \frac{5.41 \times 10^{-4} (T/\text{K})^2}{204 + (T/\text{K})}, \quad (7.7).$$

which yields bandgaps of 1.51 and 1.42 eV for samples at 77 and 300 K, respectively. The bandgap “knee” is visible in the QE spectral plots of Fig. 7.27 only for 77 K results. More noteworthy is the significant increase in ESP observed for all three samples cooled to 77 K. The ESP for the highly-doped sample increased from ~30 to 41 %, and from ~ 40 to 52 % for the low-doped sample. This behavior is consistent with Fig. 7.25, which predicts smaller spin relaxation rates for both mechanisms (BAP and DP) at lower temperature. For the low-doped sample at 77 K, measured polarization exceeds the theoretical maximum value of 50 %. This could point to an inaccurate effective Sherman Function used in the Mott polarimeter analysis, with this measurement serving to identify the magnitude of systematic error relevant to the entire study, or perhaps an indication of some interesting physics phenomenon, e.g., the creation of strain within the sample at cryogenic temperature, which serves to eliminate the energy level degeneracy of the P<sub>3/2</sub> ground state.

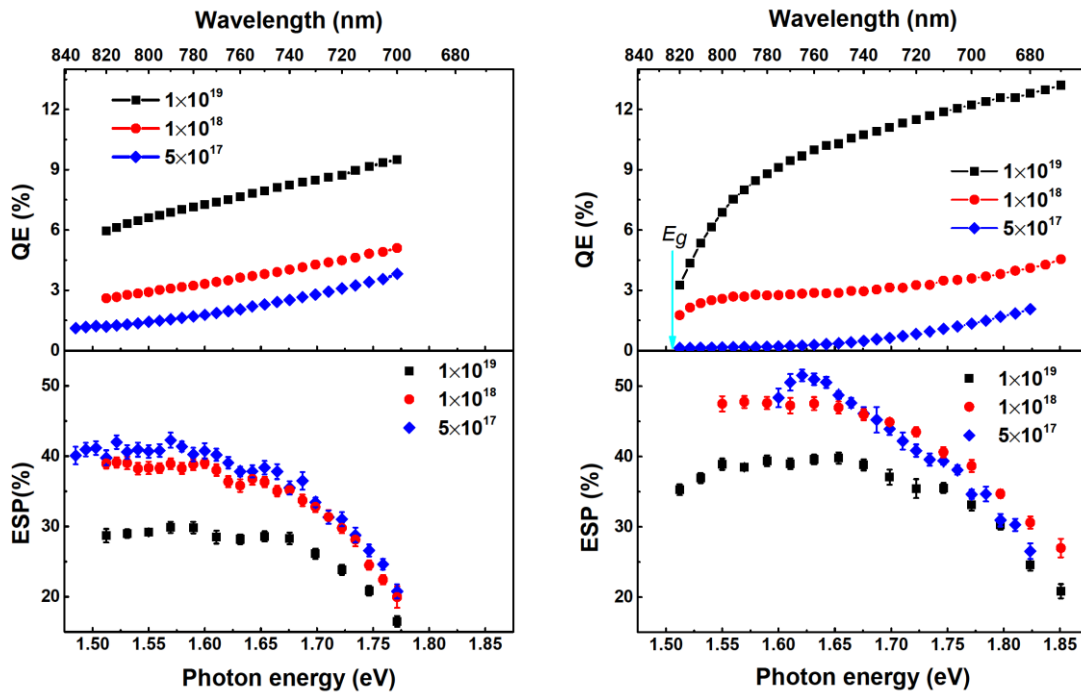


**Fig. 7.27** The QE and ESP of bulk GaAs (100 cleave plane) with different Zn dopant densities, and measured at 300 K (left) and 77 K (right). Error bars are statistical. Axes ranges were kept identical to highlight the measurement variations observed between conditions. The bandgap energy  $E_g$  could be discerned for samples at 77 K (note arrow)

The **temperature** and **dopant density** studies are summarized in Fig. 7.28, which shows ESP versus temperature for the three samples with different dopant concentrations. Overall, lower temperature leads to lower spin relaxation rate, and therefore higher ESP. Fits were applied to the data sets using the sum of expressions (7.4) and (7.6), which describe the DP and BAP spin relaxation mechanisms, respectively. The fit to the high-dopant sample set is quite good, but less so for the lower dopant density results, although the fits still support the basic predicted trend.

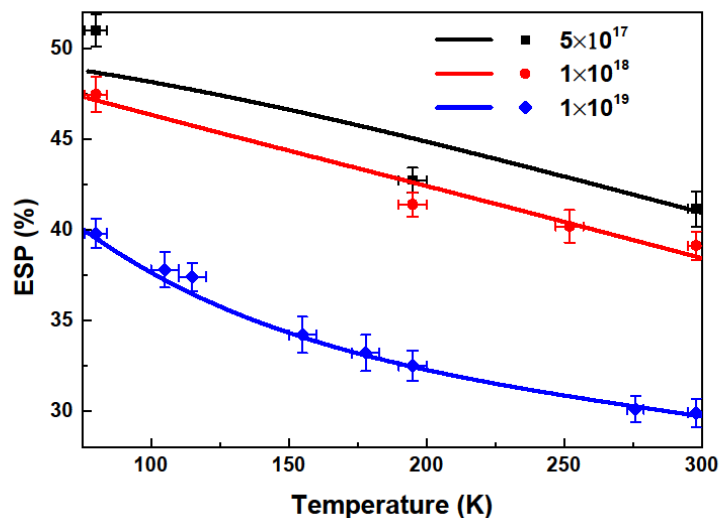


**Fig. 7.28** Maximum ESP versus sample temperature and dopant density (the wavelength of illumination was allowed to vary to provide peak polarization). Fits were applied using the sum of expressions (7.4) and (7.6), which describe the DP and BAP spin relaxation mechanisms, respectively. Vertical error bars are statistical; horizontal error bars relate to uncertainty in sample temperature

### High Polarization Strained-Superlattice Photocathode with Distributed Bragg Reflector

GaAs photocathodes grown on a crystal structure with a different lattice constant can provide beam polarization exceeding 50% because of induced uniaxial strain that eliminates the degeneracy of the  $P_{3/2}$  valence band. The first demonstrations of this technique were reported in 1991 using photocathodes grown with a single strained layer [113,114]. Throughout the 1990s, single-strained-layer GaAs/GaAsP photocathodes [114,115] [116] were used at electron accelerators throughout the world [89,94,99] providing polarization 75 %-80 % and maximum QE  $\sim$  0.3 % or less. But beam delivery using single-strained-layer photocathodes made apparent the delicate competing balance between maintaining the required strain, and growing a layer thick enough to provide sufficient QE. In the following decade, higher polarization and notably higher QE were obtained using **strained superlattice** structures consisting of very thin quantum-well active layers and alternating lattice-mismatched barrier layers [117]. The superlattice structure maintained the required degree of strain to produce high polarization and also provided sufficient active layer thickness to obtain higher QE. The first demonstration of beam production from a strained GaAs/In<sub>0.15</sub>GaAs superlattice photocathode in 1994 achieved polarization of 82.7 % but QE of just 0.015 %; however, continued development eventually resulted in photocathodes with QE  $\sim$ 1 %. The strained GaAs/GaAsP<sub>0.36</sub> superlattice structure reported in [118] provided QE of 1.2 % with polarization of 86 % and is available commercially [119]. Strained superlattice photocathodes fabricated at other facilities have also demonstrated very high polarization but no higher QE [120-123].

Some new accelerator applications require very high average current polarized beams. A photocathode with a QE of only 1% would require  $\sim$  8 W of laser light (with RF structure) to generate the desired 50 mA average beam current for the eRHIC proposal [124] and even more light when QE decays during operation due to ion-bombardment [125]. In the standard strained superlattice design, most of the incident laser light simply heats the photocathode instead of promoting electron ejection, which can degrade QE due to evaporation of the chemicals used to reduce the surface work function. Methods to cool the photocathode during beam delivery are complicated because the photocathode floats at high voltage. Developing photocathodes with enhanced QE could simplify the photogun design, reduce the drive-laser power requirements and prolong the effective operating lifetime of the photogun.

A photocathode with a **distributed Bragg reflector (DBR)** was first proposed in 1993 [126] and reported in following years [127] [128] as a means to enhance photocathode QE. The DBR serves to create a Fabry-Perot cavity formed by the front surface of photocathode and a DBR region existing beneath the superlattice active layer. Instead of a single pass in the standard design, laser light of a particular wavelength reflects repeatedly within the Fabry-Perot cavity, which increases the beneficial absorption of the incident photons, and in principle leads to enhanced QE. From past work, it was clear that the wavelength of peak reflectivity of the DBR was very sensitive to the refractive indices and thickness of each DBR layer constituent, and that the peak of resonant absorption was very sensitive to the thickness of the photocathode, especially the spacer layer between the DBR and the superlattice

photocathode structures. Accurate control of the thickness of each layer and of the composition of each constituent chemical within the photocathode structure represents a significant challenge.

A recent DBR study [129] benefited from past work that resulted in the fabrication of the strained **GaAs/GaAsP** superlattice photocathode described in [118], which represents the basis for polarization and QE comparison. See [118] for a complete description of the design criteria and optimization of this photocathode structure. A schematic layout of the strained GaAs/GaAsP superlattice photocathodes with and without DBR structure is shown in Fig. 7.29.

GaAs	5 nm	$p=5 \times 10^{19} \text{ cm}^{-3}$	GaAs	5 nm	$p=5 \times 10^{19} \text{ cm}^{-3}$
GaAs/GaAsP SL	(3.8/2.8 nm) $\times 14$	$p=5 \times 10^{17} \text{ cm}^{-3}$	GaAs/GaAsP SL	(3.8/2.8 nm) $\times 14$	$p=5 \times 10^{17} \text{ cm}^{-3}$
GaAsP <sub>0.35</sub>	2750 nm	$p=5 \times 10^{18} \text{ cm}^{-3}$	GaAsP <sub>0.35</sub>	750 nm	$p=5 \times 10^{18} \text{ cm}^{-3}$
Graded GaAsP <sub>x</sub> (x = 0~0.35)	5000 nm	$p=5 \times 10^{18} \text{ cm}^{-3}$	GaAsP <sub>0.35</sub> /AlAsP <sub>0.4</sub> DBR	(54/64 nm) $\times 12$	$p=5 \times 10^{18} \text{ cm}^{-3}$
GaAs buffer	200 nm	$p=2 \times 10^{18} \text{ cm}^{-3}$	GaAsP <sub>0.35</sub>	2000 nm	$p=5 \times 10^{18} \text{ cm}^{-3}$
p-GaAs substrate ( $p>10^{18} \text{ cm}^{-3}$ )			p-GaAs substrate ( $p>10^{18} \text{ cm}^{-3}$ )		

**Fig. 7.29** Schematic structure of the photocathodes: without DBR (left) and with DBR (right)

The DBR was composed of multiple layers of alternating high and low index of refraction. A natural choice for high index of refraction layer was GaAsP, which provides a good lattice match to the graded buffer layer. Though a challenge for growth, AlAs<sub>1-y</sub>P<sub>y</sub> was chosen for the low index-of-refraction layer, in order to achieve maximum refractive index contrast and minimum DBR thickness. The thickness of each layer follows the quarter-wavelength condition [126]:  $n_H(\lambda_{DBR})d_H = \frac{\lambda_{DBR}}{4} = n_L(\lambda_{DBR})d_L$ . The bandwidth for which the DBR exhibits high reflectivity is given by the formula:

$$\Delta\lambda_{DBR} = \frac{4\lambda_{DBR}}{\pi} \sin^{-1} \left( \frac{n_H(\lambda_{DBR}) - n_L(\lambda_{DBR})}{n_H(\lambda_{DBR}) + n_L(\lambda_{DBR})} \right). \quad (7.8)$$

The **Fabry-Perot cavity** is formed by the vacuum/GaAs cap layer interface and the DBR. Proper thickness of a GaAsP spacer layer between GaAs/GaAsP superlattice and the DBR ensures the maximum absorption in the superlattice active layer and coincides with the central reflective wavelength of the DBR. To design the structure, the refractive index of these layers can be estimated using the simplified interband transition model as a function of photon energy [130]:

$$n(E)^2 = A \left[ f(X_0) + \frac{1}{2} \left( \frac{E_0}{E_0 + \Delta_0} \right)^2 f(X_{S0}) \right] + B, \quad (7.9)$$

with  $f(X) = X^{-2}(2 - \sqrt{1+X} - \sqrt{1-X})$ ,  $X_0 = \frac{E}{E_0}$ , and  $X_{S0} = \frac{E}{E_0 + \Delta_0}$ . Here,  $A$  represents the strength parameter of the  $E/(E_0 + \Delta_0)$  terms and  $B$  represents the nondispersive contribution arising from the higher-lying band-gap terms ( $E_1, E_1 + \Delta_1, E_2, \text{etc.}$ ) for each layer. The quantities  $E_0$  and  $\Delta_0$  are the

band-gap energy and spin-orbit splitting, respectively, given by Vegard's Law for  $\text{GaAs}_{1-x}\text{P}_x$  [131] [132].

The desired wavelength of peak reflectivity was  $\lambda_{DBR} \sim 780$  nm, compatible with CEBAF drive lasers. Setting the phosphorus fractions in the  $\text{GaAs}_{1-x}\text{P}_x$  and  $\text{AlAs}_{1-y}\text{P}_y$  layers to 0.35 and 0.4, respectively, provided refractive indices of  $n_H(780 \text{ nm}) = 3.4506$  and  $n_L(780 \text{ nm}) = 2.9443$ . From these parameters, the design values for the thickness of the  $\text{GaAsP}_{0.35}$  and  $\text{AlAsP}_{0.4}$  layers were 56.5 nm and 66.5 nm, respectively. Actual layer thicknesses were very close to these design values, 54 nm and 64 nm, which set the wavelength of peak reflectivity to  $\lambda_{DBR}$  of 755 nm, and the reflectivity bandwidth  $\Delta\lambda_{DBR} \sim 79$  nm. This implies that the DBR can achieve a high reflectivity,  $> 90\%$  for wavelengths between 715 and 795 nm.

The **transfer matrix method** [133]-[134] was used to calculate the reflection, transmission and absorption of incident light through the complete multilayer thin-film structure including the GaAs substrate. Calculated values of surface reflectivity ( $R$ ), transmittance ( $T$ ) into the GaAs substrate, absorption ( $A$ ), and the absorption enhancement factor as a function of wavelength, are shown in Fig. 7.30. There are two **resonant absorption** peaks within the optical cavity for the DBR photocathode at wavelengths 726 nm and 776 nm. Absorption by the substrate is not plotted, as this process does not contribute to the polarized electron emission. The resonant peak at 776 nm is just 4 nm from the desired value 780 nm. At 776 nm, corresponding to maximum electron spin polarization, the absorption is 21.03 %, surface reflectivity is 50.14 %, and transmittance into the GaAs substrate is 28.83 %. The full-width-at-half-maximum of the Fabry-Perot resonance is about 10 nm at 776 nm. The absorption enhancement factor is 7.4 at this wavelength.

To estimate the quantum efficiency of the photocathode, one can solve the one-dimensional diffusion equations [135]-[136], based on Spicer's three-step model:

$$QE(\lambda) = \frac{P_L F_L A}{1 + \frac{1}{\alpha_\lambda L_L}} + \frac{P_\Gamma \exp[k(\frac{1}{1.42} - \frac{\lambda}{1240 \text{ nm}})] A}{1 + \frac{1}{\alpha_\lambda L_\Gamma}} [F_\Gamma + \frac{F_L L_\Gamma}{\alpha_\lambda F_L (L_\Gamma + L_L)(1 + \frac{1}{\alpha_\lambda L_L})}] \quad (7.10)$$

where  $P_\Gamma$  and  $P_L$  are the surface electron escape probabilities for the  $\Gamma$  and  $L$  minima, respectively, which are independent of the incident photon energy,  $F_\Gamma$  is the remaining fraction of excited electrons,  $F_L$  is the fraction of electrons that is excited to energies greater than the  $L$  minima,  $A$  is the absorption of photocathode,  $L_\Gamma$  and  $L_L$  are the electron diffusion lengths for the  $\Gamma$  and  $L$  minima, respectively,  $\alpha_\lambda$  is the absorption coefficient of the photocathode, and  $k$  is a coefficient ( $k \geq 0$ ). The calculated QE for the DBR photocathode, together with the QE enhancement factor as a function of wavelength, are shown in Fig. 7.30.

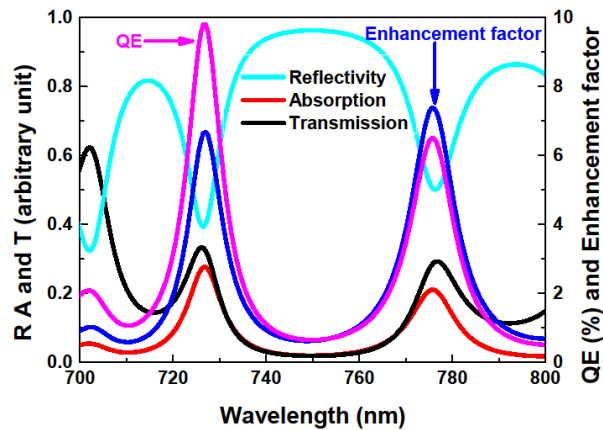


**Fig. 7.30** Calculated values of absorption, reflectivity and transmittance of the DBR photocathode, as a function of wavelength. Also shown, calculated QE and the QE enhancement factor compared to the photocathode without the DBR

Measured values of QE and polarization as a function of wavelength, for photocathodes with and without DBR, are shown Fig. 7.31a. For the non-DBR photocathode, results are consistent with past work [118] indicating peak polarization of 90 % and QE of 0.89 % at a wavelength  $\sim 780$  nm. In stark contrast, the QE of the DBR photocathode shows the telltale prominent oscillatory behavior indicative of resonant absorption. Measured reflectivity and QE enhancement (i.e., the ratio of QE values of photocathodes with and without DBR) are shown in Fig. 7.31b. The two dips in the reflectivity spectrum are clearly correlated with wavelength locations of QE maxima. At the wavelength of interest, 776 nm, the QE was 6.4 % and polarization  $\sim 84$  %. The measured QE enhancement of  $\sim 7.2$  is very close to the predicted value of  $\sim 7.4$ .

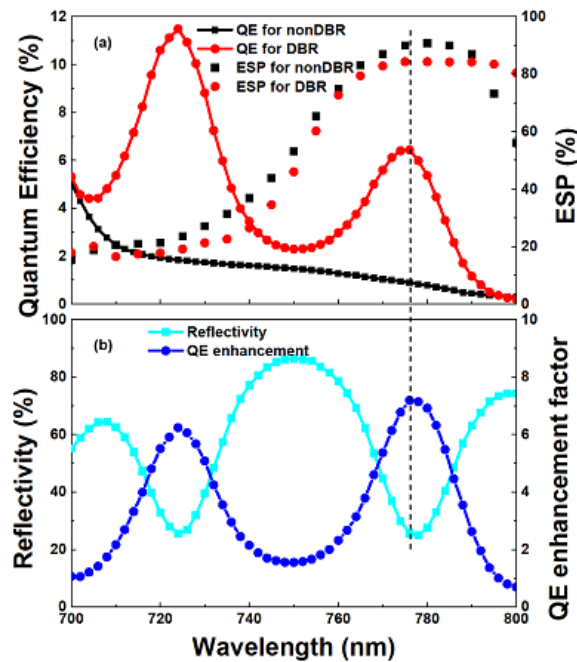


**Fig. 7.31** (a) The QE and electron-spin polarization (ESP) for the strained GaAs/GaAsP superlattice photocathodes with and without DBR as a function of the wavelength; (b) Reflectivity and QE enhancement factor of DBR photocathode as a function of the wavelength. The dashed line indicates the resonant position

## Ion Bombardment – Cleave Plane Dependence

**Ion back-bombardment** represents the dominant lifetime-limiting mechanism of modern DC high voltage photoguns that rely on delicate NEA GaAs photocathodes [125] [137]. Ion back-bombardment is the process whereby residual gas within the cathode/anode gap is ionized by the extracted electron beam and attracted to the negatively-biased photocathode. Photogun experts speculate that ions strike the photocathode surface sputtering away the chemicals used to create the NEA condition, or they become implanted within the photocathode material, knocking out atoms from the crystal structure and altering the energy band structure, or they serve as interstitial defects that reduce the electron diffusion length. All of these possibilities are problematic because the net result is reduced QE, which results in reduced operating lifetime of the photogun. Improving the vacuum within the photogun is the best way to reduce ion back-bombardment and thereby prolong the operating lifetime of the photogun, but modern DC high voltage photoguns are already operating in the  $10^{-11}$  Torr (about  $10^{-9}$  Pa) pressure range, or lower, so improving the photogun vacuum further is thus very challenging.

To understand ion back-bombardment inside a photogun, it is important to note that the energy spectrum of the extracted photoemitted electron beam within the cathode/anode gap is broad, with electrons leaving the cathode electrode at zero velocity, and then gaining energy until reaching the anode. For a typical DC high voltage photogun, the photocathode is biased at voltages between  $-100$  and  $-350$  kV. Hydrogen is the dominant gas species inside a modern photogun, and the peak **ionization cross section** occurs at  $\sim 100$  V and drops by more than two orders of magnitude at  $100$  kV [138] (Fig. 7.32). So in typical photogun operation, the surface of the photocathode is bombarded by significantly more low-energy ions than high-energy ions.

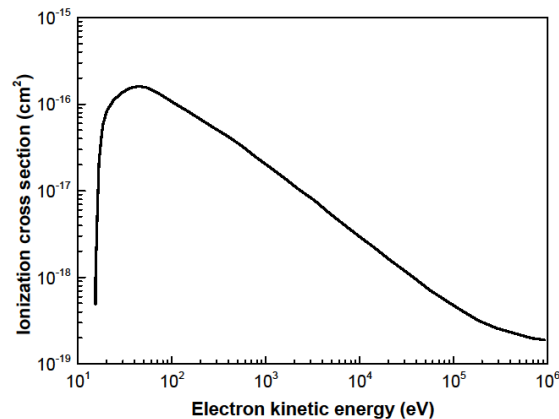


**Fig. 7.32** Electron impact ionization cross section for hydrogen molecules - the dominant gas species inside modern DC high voltage photoguns - as a function of electron kinetic energy

The software program SRIM (Stopping Range of Ions in Matter) [139] can be used to estimate the penetration depth of the hydrogen ions into the material and the number of vacancies created within the material when ions collide with gallium and arsenic atoms and knock them out of their positions within the crystal lattice. In the simulation, the hydrogen ions were injected into GaAs at normal incidence and the ion injection energy was varied from  $100$  V to  $10$  kV while keeping the ion dose constant for each simulation. The stopping depth of implanted hydrogen ions and the distribution of

knock-out vacancies for different ion energies are shown in Fig. 7.33. Unsurprisingly, higher energy ions penetrate deeper into the material and do more damage to the crystal structure, compared to lower energy ions. The **penetration depths** (defined as the depth at which the dose falls to 1/e of its original value) are 69 Å and 1690 Å for 100 V and 10 kV hydrogen ions, respectively, while gallium and arsenic atoms begin to be knocked out from their lattice positions at ion energies greater than ~ 500 V. It is an interesting question, which ions are most problematic for NEA GaAs photocathodes inside a photogun, many low-energy ions or fewer high-energy ions [140] ?

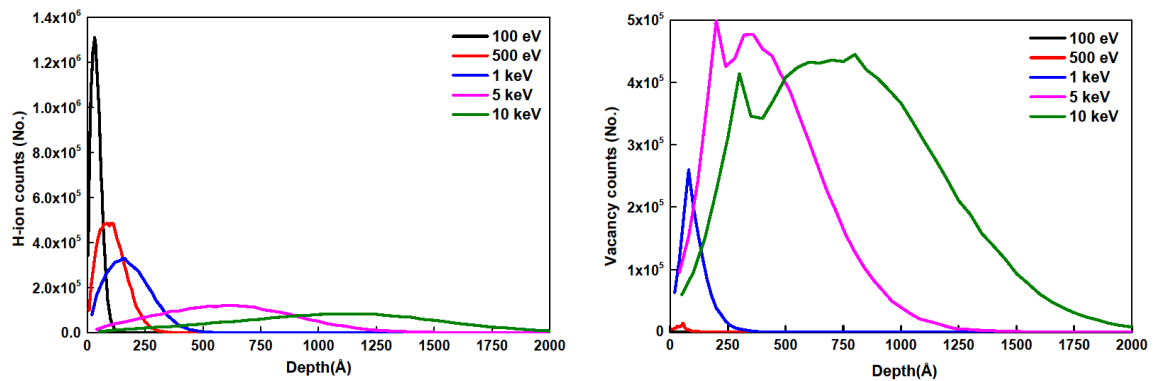


**Fig. 7.33** (Left) Hydrogen ion distribution and (right) vacancy distribution within GaAs, for different hydrogen ion energies. All simulations performed using the same hydrogen ion dose of  $8.1 \times 10^5 \text{ nA} \cdot \text{s}$ . Plots obtained using SRIM [139]

Channeling is the process whereby positively charged ions follow the direction between two neighboring crystal planes, which leads to deeper penetration of the positive ions in the material. Figure 7.34 shows the relative spacing of atoms in the GaAs crystal structure for the three **surface cleave planes** studied, viewed at normal incidence. The red boxes in Figure 7.33 denote the recurring geometric cells used for calculating the atomic number density (number of atoms per unit area), which is a measure of the “open space” between atoms. The atomic number densities for the (100), (110) and (111A) GaAs cleave planes were calculated to be  $8/a^2$ ,  $4\sqrt{2}/a^2$ , and  $4\sqrt{3}/a^2$ , respectively, where  $a$  is the GaAs lattice constant ( $5.6535 \text{ Å}$ ). Measurements were performed to investigate if channeling would be enhanced for the (110) cleave plane which possesses the smallest atomic number density (i.e., the most open space between atoms). If so, a photocathode with (110) surface cleave plane would therefore be the most insensitive to ion bombardment.

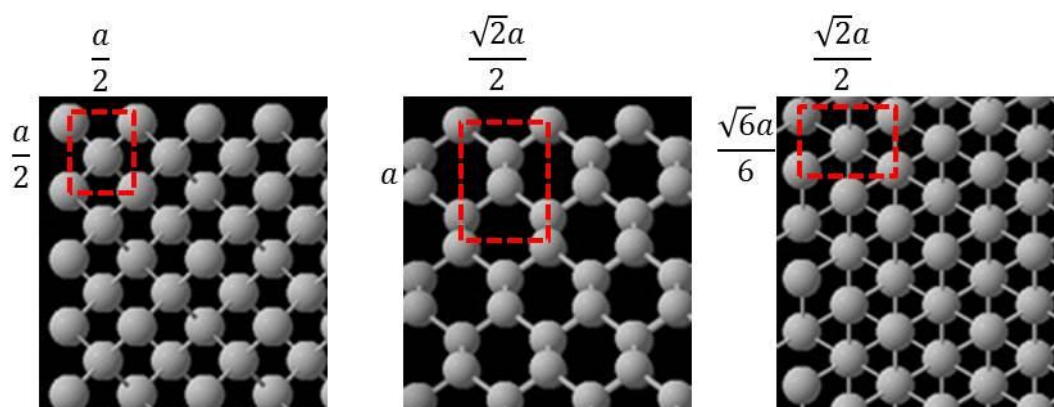


**Fig. 7.34** Schematic representations of the GaAs crystal for three surface cleave planes, looking normal to the surface – from left to right, (100), (110) and (111). The red boxes denote the recurring geometric cells used for calculating the atomic number density for each cleave plane and  $a$  is the GaAs lattice constant.

To quantify the effects of ion energy, and to investigate whether crystal orientation plays a role in QE degradation, GaAs samples with different surface cleave planes were implanted with hydrogen ions at 100 V and 10 kV. Prior to implantation, each photocathode sample was heated, cooled and activated. The QE was measured as a function of laser wavelength and the results are presented in Fig. 7.35. Quantum efficiency was calculated using the expression  $QE = 124I/P\lambda$ , where  $I$  is the measured photocurrent in  $\mu\text{A}$ ,  $P$  is the laser power in mW, and  $\lambda$  is the wavelength of the laser light in nm [141]. The cleave planes (100) and (110) provided the highest QE, approximately 21 % at the laser wavelength 532 nm. Cleave plane sample (111A) provided the lowest QE, approximately 19 % at 532 nm. Although these values are lower than reported in [97], the relative trend between samples is consistent (i.e.,  $QE_{100} > QE_{110} > QE_{111A}$ ).

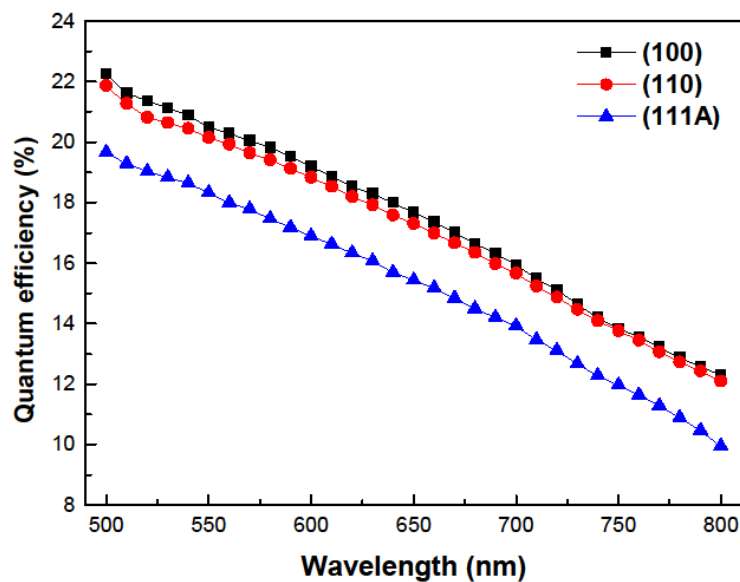


**Fig. 7.35** Photocathode QE versus laser wavelength for commercial bulk GaAs samples with different surface cleave planes, prior to ion implantation

After determining that each sample provided high QE, samples were heated to 250 °C for 20 minutes to remove the activation layer of Cs and  $\text{NF}_3$ . Samples were then cooled to room temperature and implanted with hydrogen ions at the chosen energy and for the prescribed dose. The vacuum was allowed to recover overnight. Photocathode samples were then repeatedly heated and activated following different heating protocols (temperature and duration). Following each activation, the photocathode QE was measured at 532 nm and compared to the pre-implantation value. In this manner, the sample's sensitivity to ion damage was evaluated. Figure 7.36 shows typical QE maps for samples implanted with 100 V and 10 kV hydrogen ions (the caption provides specific details of the cleave plane surface and heating protocol). For 100 V ions, QE degradation was uniformly distributed across the sample. But for 10 kV hydrogen ions, the QE degradation was localized to a specific region of the sample, consistent with an electrostatic simulation that predicted significant focusing.

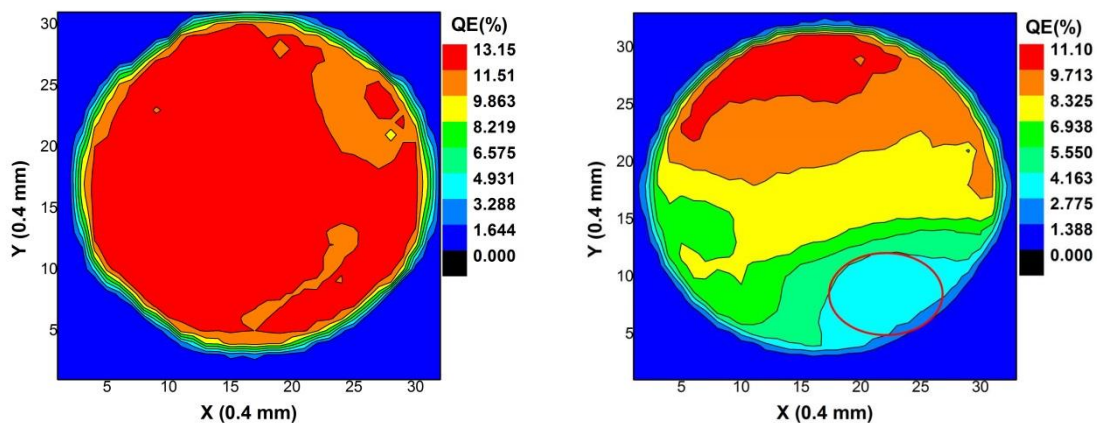


**Fig. 7.36** Typical QE maps of the photocathode obtained by scanning a focused low power green laser beam across the photocathode following activation. These maps show the bulk GaAs (111A) sample. Left: after the third activation following implantation with 100 V hydrogen ions. Right: after the third activation following implantation with 10 kV hydrogen ions. The 2-dimensional plots help to illustrate ion implantation uniformity: 100 V hydrogen ions were uniformly distributed across the entire sample but 10 kV hydrogen ions were focused to a region denoted by the ellipse, consistent with the particle tracking code simulations

Figure 7.37 summarizes the results of the experiment, with QE at 532 nm plotted as a function of repeated activation following a variety of heating protocols described within the caption, for samples implanted with 100 V and 10 kV hydrogen ions, and for samples that were not implanted with ions. When samples were repeatedly heated and activated – but not subjected to **hydrogen ion implantation** – the QE at 532 nm remained constant to within 5%. This speaks to the quality of the vacuum within the apparatus, which was dominated by chemically inert gas species like H<sub>2</sub>, CH<sub>4</sub>, CO and CO<sub>2</sub>. The QE of each sample did not degrade following repeated heating and activation, due to adverse chemical reactions that might take place under degraded vacuum conditions, especially when samples were hot.

The next observation evident in Fig. 7.37 is that both 100 V and 10 kV hydrogen ions served to degrade the sample QE, however the QE degradation associated with 10 kV ions was significantly greater than that caused by 100 V ions. In general, for both ion energies, heating the sample to higher temperature and for longer time served to **restore QE**. For implantation with 100 V hydrogen ions, the QE could be completely restored by heating the sample. But for implantation with 10 kV hydrogen ions, only a fraction of the QE could be restored. It should be noted that data points presented in Figure 7.37 were obtained by averaging the QE measurements over a specific region of the photocathode sample surface. For 100 V ion implantation, QE measurements were averaged over the entire sample. For the 10 kV ions, QE values were averaged only in the region where the ions were focused, as indicated by the ellipse shown in Fig. 7.36 (right).

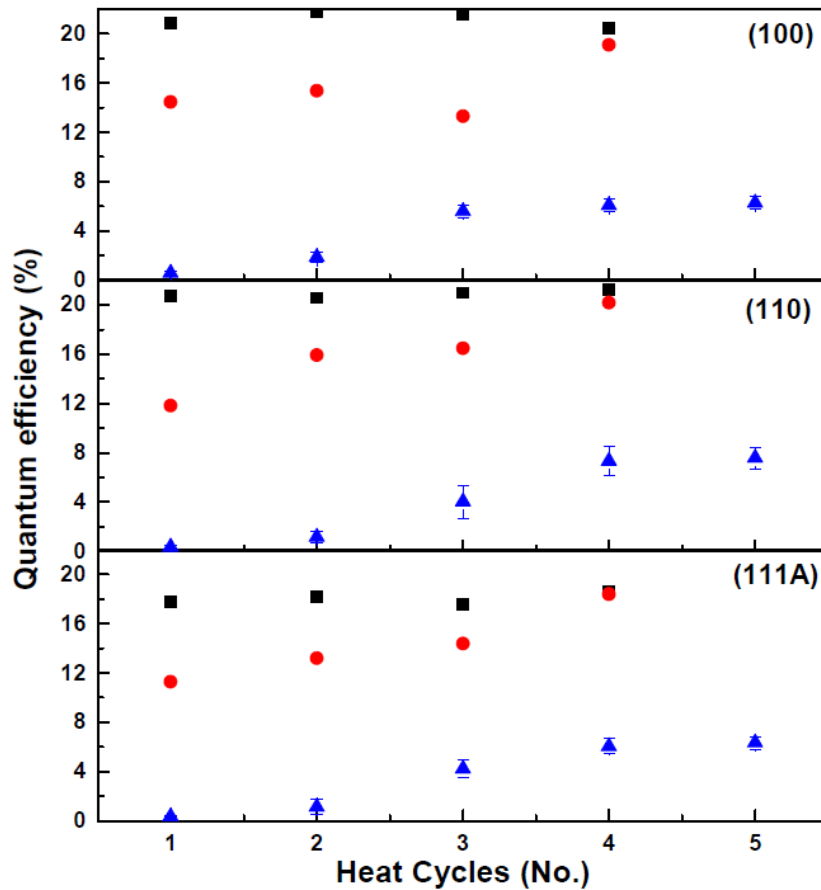


**Fig. 7.37** QE versus heat cycle for bulk GaAs with three different surface cleave planes. Black Square: no implantation; Red Circle: implantation with 100 V hydrogen ions; Blue Triangle: implantation with 10 kV hydrogen ions. Error bars represent the standard deviation in QE values averaged over the entire sample for “no implantation”: and 100 V results, and over the small region denoted by the red circle in Fig. 7.36 (right) for the 10 kV results. Error bars are smaller than the data-point symbols for “no implantation” and 100 V results, because QE was very uniform across the sample. Heat cycles were: number 1: 250 °C for 20 minutes; 2: 370 °C for 30 minutes; 3: 490 °C for 1 hour; 4 and 5: 550 °C for 1 hour

To determine if a specific surface cleave plane provided enhanced **ion channeling**, the QE results from the 10 kV ion implantation studies were divided by the non-implantation QE results (Fig. 7.38). In accordance with supposition, when ions penetrate deeper into the material, they pass beyond the surface region that contributes to photoemission and therefore provide less QE degradation. When comparing QE values of implanted and non-implanted samples, those with the highest QE ratio would correspond to samples with enhanced ion channeling. The simple picture presented in Fig. 7.34 suggests samples would be ordered (110), (111A), (100), from highest to lowest levels of channeling. This simple picture is consistent with results presented in Fig. 7.38, at least for samples that were heated sufficiently long and at a relatively high temperature (see results for heat cycles 4 and 5 in Fig. 7.38). The (110) GaAs cleave plane—i.e., the sample with the most “open space” between atoms, and therefore the sample supporting the highest level of ion channeling—exhibited the highest **QE ratio**. By contrast, the cleave plane (100)—i.e., the sample with the least “open space” between atoms, and therefore the sample supporting the lowest level of ion channeling—exhibited the lowest QE ratio. If one assumes a strict QE dependence on atomic number density, the QEs of the (110) and (111A) cleave

planes following ion implantation should be greater than the (100) sample by roughly 41 % and 15 %, respectively. In comparison, looking at Fig. 7.38 heat cycle 5 values, the measured QEs of the (110) and (111A) cleave planes following ion implantation are greater than sample (100) by 33 % and 30 %, respectively. However, there is fairly good agreement between measurements and predictions when error bars are taken into account.

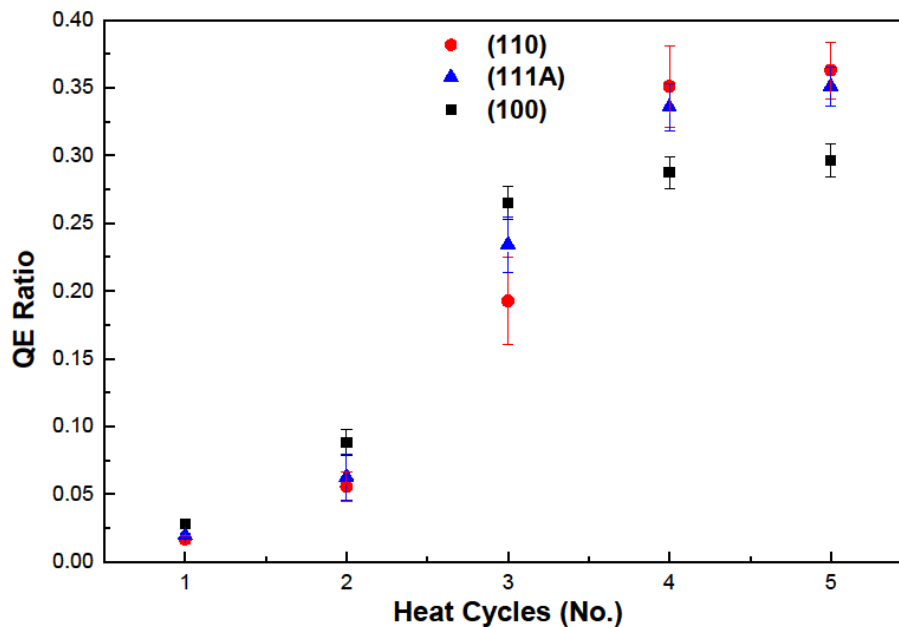


**Fig. 7.38** QE ratio, for samples implanted with 10 kV hydrogen ions to samples that were not exposed to hydrogen ions, as a function of heat cycle, for bulk GaAs with three different surface cleave planes. Heat cycle numbers: 1: 250 °C for 20 minutes; 2: 370 °C for 30 minutes; 3: 490 °C for 1 hour; 4 and 5: 550 °C for 1 hour

In conclusion, implantation of the photocathode with either low or high energy hydrogen ions served to reduce photocathode QE, but the QE degradation caused by 100 V hydrogen ions was modest and QE could easily be recovered following sample heating. In sharp contrast, the QE degradation caused by 10 kV hydrogen ions was severe and QE could not be fully recovered with heat. These observations suggest that low energy ions penetrate the surface, stopping at locations between atoms and creating interstitial defects that likely reduce the diffusion length of the electrons within the material, reducing the number of available electrons that reach the photocathode surface that can contribute to photoemission. During sample heating, the **interstitial defects** diffuse throughout the material, restoring the electron diffusion length and the photocathode QE. Whereas high energy ions likely generate knock-out **vacancies** within the crystal structure that permanently adversely alter the band structure of the semiconductor. As noted above, inside a DC high voltage photogun, the photocathode will be bombarded by considerably more low voltage ions than high voltage ions. This is fortuitous and explains why the photocathode QE can be routinely restored following simple heating and reactivation, except at the electrostatic center of the photocathode, where the highest energy ions are directed [137].

In addition, the data support the simple picture that channeling is enhanced for the sample with the most “open space” between atoms. More “open space” leads to enhanced channeling, which means

high-energy ions create fewer vacancies that lead to reduced and unrecoverable QE. The surface cleave plane (110) has the most “open space”, and cleave plane (100) the least “open space”. As such, the surface cleave plane (110) was the least sensitive to ion bombardment and the cleave plane (100) the most sensitive.

Considering all the results in total, the best choice for a photogun using bulk GaAs would be surface cleave plane (110), since this provides the highest QE and the least sensitivity to ion bombardment. It's true that modern high-current accelerator applications now prefer alkali-antimonide photocathodes over GaAs photocathodes, because alkali-antimonide photocathodes offer similarly high QE but longer operating lifetime. However, spin-polarized accelerator applications may be forced to use bulk GaAs as the only practical means to generate milliampere-levels of spin-polarized beam current.

## Conclusion

Photocathodes represent an important technological development area, with diverse applications – from light detectors and image intensifiers to materials science and accelerator physics. There are three main classes of photocathode used today – metals, semiconductors with positive electron affinity (PEA) and semiconductors with negative electron affinity (NEA). Metals are rugged, tolerant of poor vacuum and emit electrons promptly upon absorbing a photon (within 10s of fs). However, metals have typically poor quantum efficiency ( $\sim 10^{-5}$ ) and are only sensitive to UV light. PEA semiconductors generally have much higher QE, as the loss of excited carriers is reduced by the elimination of electron-electron scattering, at least for a range of photon energies. The two most common PEA semiconductors are Cs<sub>2</sub>Te and the alkali antimonide family – Cs<sub>2</sub>Te is a near UV sensitive cathode that can have very high QE (>20%) [142], while the alkali antimonides typically have very high QE peaked in the blue [143]. PEA semiconductors typically require good vacuum (nTorr) and have response times  $\sim 0.5$  ps. NEA semiconductors, such as the GaAs family, can have very good QE over a broad range of wavelengths – even for IR light. They are also the only cathodes capable of producing significant spin polarization in the emitted electron beam. However, these cathodes rely on a dipole monolayer on the surface to achieve NEA, and are therefore very sensitive to poor vacuum (typically  $\sim 1$  pTorr). They can also have long response times (>100ps). Many accelerator applications, especially electron colliders and free electron lasers, use photocathodes as the electron source, and these machines typically drive the development of the state of the art in this field. Improvement directions are higher QE, high peak current densities in the pulsed beam of  $> 10^5$  A/cm<sup>2</sup> and high beam currents of more than 50 mA.

## References

- [1] W. Schattke, *Prog. Surface Sci.* **54**, 211 (1997).
- [2] C. N. Berglund and W. E. Spicer, *Phys. Rev. A* **136**, A1030 (1964).
- [3] W. E. Spicer, *Phys. Rev.* **112**, 114 (1958).
- [4] W. E. Spicer and A. Herrera-Gomez, *Modern theory and applications of photocathodes*, Report No. SLAC-PUB-6306 SLAC/SSRL-0042, 1993.
- [5] G. Ferrini *et al.*, *Solid State Comm.* **106**, 21 (1998).
- [6] W. E. Pickett and P. B. Allen, *Phys. Letters* **48A**, 91 (1974).
- [7] J. Smedley *et al.*, *Phys. Rev. ST Accel. Beams* **11**, 013502 (2008).
- [8] D. H. Dowell *et al.*, in *FEL'07 Novosibirsk, Russia*, (2007), p. 276.
- [9] D. H. Dowell *et al.*, *Phys. Rev. ST Accel. Beams* **9**, 063502 (2006).
- [10] G. Suberlucq, *Developpement et production de photocathodes*, Report No. CLIC-NOTE-299, 1996.
- [11] H. B. Michaelson, *Journal of Applied Physics* **48**, 4729 (1977).
- [12] E. Chevallay *et al.*, *Nucl. Instr. Meth. Phys. Res. A* **340**, 146 (1994).
- [13] F. L. Pimpec *et al.*, in *IPAC 2010 Kyoto, Japan*, (2010), p. 2233.
- [14] T. Srinivasan-Rao *et al.*, *J. Appl. Phys.* **69**, 3291 (1991).
- [15] R. Valizadeh *et al.*, in *IPAC2014 Dresden, Germany*, (2014), p. 711.
- [16] P. Schoessow *et al.*, *The Argonne wakefield accelerator high current photocathode gun and drive linac.*, Report No. ANL-HEP-CP-95-34, 1995.
- [17] J. Bossert *et al.*, in *36th international Free Electron Laser Conference FEL14*, edited by JaCow Basel, Switzerland, (2014), p. 832.
- [18] S. Mistry *et al.*, in *IPAC2015 Richmond, VA, USA*, (2015), p. 1759.
- [19] A. Brachmann *et al.*, in *IPAC2011 San Sebastian, Spain*, (2011), p. 3200.
- [20] F. Zhou *et al.*, *Phys. Rev. ST Accel. Beams* **15**, 090703 (2012).
- [21] X. J. Wang *et al.*, in *LINAC1994 Tsukuba, Japan*, (1994), p. 407.
- [22] L. N. Hand and U. Happek, *Nucl. Instr. Meth. Phys. Res. A* **372**, 335 (1996).
- [23] Y. Gao and R. Reifengerger, *Phys. Rev. B* **35**, 4284 (1987).
- [24] D. H. Dowell, in *FEL2010 Malmoe, Sweden*, (2010).
- [25] C. Vicario *et al.*, in *FEL 2013 New York, USA*, (2013), p. 434.
- [26] R. J. Reid, *Cleaning for vacuum service*, Report No. CERN-OPEN-2000-276, 1999.
- [27] J. D. Herbert and R. J. Reid, *Vacuum* **47**, 693 (1996).
- [28] R. Ganter *et al.*, in *FEL 2013 New York, NY, USA*, (2013), p. 259.
- [29] P. H. Holloway and G. E. McGuire, *Handbook of Compound Semiconductors* (William Andrew 1996).
- [30] H. Qian *et al.*, in *PAC2009 Vancouver, Canada*, (2009), p. 476.
- [31] G. Penco *et al.*, in *IPAC'10 Kyoto, Japan*, (2010), p. 1293.
- [32] F. Zhou *et al.*, in *FEL'14 Basel, Switzerland*, (2014), p. 771.
- [33] <https://www.luvata.com/en/Products/Sputtering-targets-pellets-slugs/>.
- [34] Z. Zhang and C. Tang, *Phys. Rev. ST Accel. Beams* **18**, 053401 (2015).
- [35] K. L. Jensen *et al.*, *Phys. Rev. ST Accel. Beams* **17**, 043402 (2014).
- [36] A. Lorusso *et al.*, *Phys. Rev. ST Accel. Beams* **14**, 090401 (2011).
- [37] H. E. Ives, *Phys. Rev.* **38**, 1209 (1931).
- [38] E. Pedersoli *et al.*, *Appl. Phys. Lett.* **87**, 081112 (2005).
- [39] H. Tomizawa *et al.*, in *LINAC2012 Tel-Aviv, Israel*, (2012), p. 996.
- [40] M. Krueger *et al.*, *J. Phys. B: At. Mol. Opt. Phys.* **51**, 172001 (2018).
- [41] L. Wimmer *et al.*, *Nature Physics* **10**, 432 (2014).
- [42] C. Vicario *et al.*, *Optics Express* **23**, 4573 (2015).
- [43] R. Ganter *et al.*, *Phys. Rev. Letters* **100**, 064801 (2008).

- [44] J. Smedley *et al.*, J. Appl. Phys. **98**, 043111 (2005).
- [45] J. Sekutowicz *et al.*, in *PAC07* (IEEE, Piscataway, NJ, 2007), Albuquerque, NM, USA, (2007), p. 962.
- [46] A. Lorusso *et al.*, Appl. Phys. A **122**, 1 (2016).
- [47] Photocathode technology, <http://www.hamamatsu.com/jp/en/technology/innovation/photocathode/index.html> (accessed: 7 Feb 2019).
- [48] A. D. Bona and F. Sabary, J. Appl. Phys. **80**, 3024 (1996).
- [49] H. Trautner, PhD Thesis, Clic project at CERN, Switzerland, 2000.
- [50] E. Chevallay *et al.*, in *19th International Linear Accelerator Conference* Chicago, USA, (1998), p. 872.
- [51] E. Chevallay, Experimental results at the CERN photoemission laboratory with co-deposition photocathodes in the frame of the CLIC studies, Report No. CTF3-Note-104, 2012.
- [52] A. Baskaran and P. Smereka, J. Appl. Phys. **111**, 044321 (2012).
- [53] Z. Ding *et al.*, J. Appl. Phys. **121**, 055305 (2017).
- [54] P. Michelato *et al.*, in *EPAC 1996* Sitges, Spain, (1996), p. 1510.
- [55] P. Michelato, Nucl. Instr. Meth. Phys. Res. A **393**, 464 (1997).
- [56] J. Teichert *et al.*, Report on photocathodes, Report No. CARE/JRA-PHIN, July 2004, 2004.
- [57] S. H. Kong *et al.*, J. Appl. Phys. **77**, 6031 (1995).
- [58] C. Hessler *et al.*, in *IPAC15* Richmond, VA, USA, (2015), p. 1699.
- [59] B. M. v. Oerle and G. J. Ernst, Nuclear Instruments and Methods in Physics Research A **358**, 287 (1995).
- [60] S. H. Kong *et al.*, Nuclear Instruments and Methods in Physics Research A **358**, 272 (1995).
- [61] E. Chevallay *et al.*, Production of a high average current electron beam with Cs<sub>2</sub>Te photocathode, Report No. CTF3 Note 020, 2001.
- [62] S. Lederer *et al.*, in *FEL2011* Shanghai, China, (2011), p. 511.
- [63] A. R. Fry *et al.*, in *XIX International Linac Conference*, edited by F. N. A. Laboratory FERMILAB-Conf-98/272, Chicago, IL, USA, (1998), p. 642.
- [64] P. J. M. v. d. Slot *et al.*, in *FEL 2008* Gyeongju, Korea, (2008).
- [65] R. Xiang *et al.*, in *IPAC2012* New Orleans, LA, USA, (2012), p. 1524.
- [66] R. Xiang *et al.*, Phys. Rev. ST Accel. Beams **13**, 043501 (2010).
- [67] E. Prat *et al.*, in *FEL14* Basel, Switzerland, (2014), p. 970.
- [68] D. Sertore *et al.*, Nucl. Instr. Meth. Phys. Res. A **445**, 422 (2000).
- [69] S. Lederer *et al.*, in *IPAC'10* Kyoto, Japan, (2010), p. 2155.
- [70] D. H. Dowell *et al.*, Nuclear Instruments and Methods in Physics Research A **356**, 167 (1995).
- [71] B. Dunham *et al.*, Appl. Phys. Lett. **102**, 034105 (2013).
- [72] J. Smedley *et al.*, in *International Particle Accelerator Conference* Richmond, VA, USA, (2015), p. 1965.
- [73] M. Ruiz-Osés *et al.*, APL Materials **2** (2014).
- [74] S. Schubert *et al.*, APL Materials **1**, 032119 (2013).
- [75] J. Feng *et al.*, J. Appl. Phys. **121**, 044904 (2017).
- [76] C. Ghosh and B. P. Varma, J. Appl. Phys. **49**, 4549 (1978).
- [77] H. v. d. Graaf *et al.*, Nuclear Instruments and Methods in Physics Research A **847**, 148 (2017).
- [78] S. Schubert *et al.*, J. Appl. Phys. **120**, 035503 (2016).
- [79] J. Kessler, *Polarized Electrons* (2nd Edition, Springer-Verlag, Berlin 1985).
- [80] E. Leader, *Spin in Particle Physics* (Cambridge University Press 2001).
- [81] M. Kuwahara *et al.*, Appl. Phys. Lett. **105**, 193101 (2014).
- [82] M. J. Alguard *et al.*, Nucl. Instr. Meth. Phys. Res. A **163**, 29 (1979).
- [83] W. v. Drachenfels *et al.*, Nucl. Instr. Meth. Phys. Res. A **140**, 47 (1977).
- [84] M. J. Alguard *et al.*, Phys. Rev. A **16**, 209 (1977).
- [85] L. A. Hodge *et al.*, Rev. Sci. Instrum. **50**, 1 (1979).
- [86] P. F. Wainwright *et al.*, Rev. Sci. Instrum. **49**, 571 (1978).

- [87] D. T. Pierce *et al.*, Appl. Phys. Lett. **26**, 670 (1975).
- [88] C. Y. Prescott *et al.*, Phys. Lett. B **77**, 347 (1978).
- [89] E. Tsentlovich *et al.*, Nuclear Instruments and Methods in Physics Research A **582**, 413 (2007).
- [90] M. J. J. v. d. Putte *et al.*, AIP Conf. Proc., (1998), p. 260.
- [91] K. Aulenbacher *et al.*, Nuclear Instruments and Methods in Physics Research A **391**, 498 (1997).
- [92] W. Hillert *et al.*, in *AIP Conf. Proc. (Proceedings of the 14th International Symposium on High Energy Spin Physics (SPIN2000))*, edited by A. C. Proc., (2001), p. 961.
- [93] K. Wada *et al.*, in *AIP Conf. Proc. (Proceedings of the 15th International Symposium on High Energy Spin Physics (SPIN2002))*, edited by A. C. Proc., (2003), p. 1063.
- [94] C. K. Sinclair *et al.*, Phys. Rev. ST Accel. Beams **10**, 023501 (2007).
- [95] J. S. Blakemore, J. Appl. Phys. **53**, R123 (1982).
- [96] D. T. Pierce and F. Meier, Phys. Rev. B **13**, 5484 (1976).
- [97] L. W. James *et al.*, J. Appl. Phys. **42**, 4976 (1971).
- [98] T. Maruyama *et al.*, Appl. Phys. Lett. **55**, 1686 (1989).
- [99] R. Alley *et al.*, Nuclear Instruments and Methods in Physics Research A **1**, 365 (1995).
- [100] M. I. D'yakonov and V. I. Perel, ZhETF (in Russian) **60**, 1954 (1971; translated as Sov. Phys. JETP **33**, 1053 (1971)).
- [101] G. L. Bir *et al.*, ZhETF (in Russian) **69**, 1382 (1975; translated as Sov. Phys. JETP **42**, 705 (1976)).
- [102] F. Meier and B. P. Zakharchenya, *Optical Orientation* (North-Holland, Amsterdam, 1984).
- [103] P. H. Song and K. W. Kim, Phys. Rev. B **66**, 035207 (2002).
- [104] Y. Yafet, *Solid State Phys.* (Academic, New York, 1963), Vol. 14, p.^pp. 1.
- [105] G. Fishman and G. Lampel, Phys. Rev. B **16**, 820 (1977).
- [106] K. Zerrouati *et al.*, Phys. Rev. B **37**, 1334 (1988).
- [107] J. H. Jiang and M. W. Wu, Phys. Rev. B **79**, 125206 (2009).
- [108] I. Zutic *et al.*, Rev. Mod. Phys. **76**, 323 (2004).
- [109] A. G. Aronov *et al.*, ZhETF (in Russian) **57**, 680 (1983; translated as Sov. Phys. JETP **57**, 680 (1983)).
- [110] W. Liu *et al.*, J. Appl. Phys. **122**, 035703 (2017).
- [111] J. L. McCarter *et al.*, Nuclear Instruments and Methods in Physics Research A **618**, 30 (2010).
- [112] B. V. Zeghbrock, *Principles of Semiconductor Devices* (e-book, University of Colorado, 2011).
- [113] T. Nakanishi *et al.*, Phys. Lett. A **158**, 345 (1991).
- [114] T. Maruyama *et al.*, Phys. Rev. Lett. **66**, 2376 (1991).
- [115] T. Maruyama *et al.*, Phys. Rev. B **46**, 4261 (1992).
- [116] Bandwidth Semiconductor, <http://www.bandwidthsemi.com> (accessed: 8 Feb 2019).
- [117] T. Omori *et al.*, Jpn. J. Appl. Phys. **33**, 5676 (1994).
- [118] T. Maruyama *et al.*, Appl. Phys. Lett. **85**, 2640 (2004).
- [119] <http://www.svta.com/> (accessed: 8 Feb 2019).
- [120] A. V. Subashiev *et al.*, Appl. Phys. Lett. **86**, 171911 (2005).
- [121] X. Jin *et al.*, Appl. Phys. Lett. **105**, 203509 (2014).
- [122] Y. A. Mamaev *et al.*, Appl. Phys. Lett. **93**, 081114 (2008).
- [123] X. Jin *et al.*, Appl. Phys. Express **6**, 015801 (2013).
- [124] E. C. Aschenauer *et al.*, arXiv: 1409. 1633.
- [125] K. Aulenbacher *et al.*, U. Mainz, Operating experience with the MAMI polarized electron source, Report No. SLAC Report No. 432 (revised), 1993.
- [126] T. Saka *et al.*, Jpn. J. Appl. Phys. **32**, 1837 (1993).
- [127] J. C. Grobli *et al.*, Phys. Rev. Lett. **74**, 2106 (1995).
- [128] L. G. Gerchikov *et al.*, AIP Conf. Proc. **980**, 124 (2008).
- [129] W. Liu *et al.*, Phys. Lett. **109**, 252104 (2016).
- [130] S. Adachi, *Properties of Semiconductor Alloys: Group-IV, III-V and II-VI Semiconductors* (Wiley, 2009), p.^pp. 238.
- [131] M. Levinshtein *et al.*, *Handbook series on semiconductor parameters* (World Scientific,, 1996).
- [132] I. Vurgaftman *et al.*, J. Appl. Phys. **89**, 5815 (2001).

- [133] H. A. Macleod, *Thin-film Optical Filters (4th edition)* (CRC Press, Baton Rouge, 2010).
- [134] P. Peumans *et al.*, J. Appl. Phys. **93**, 3693 (2003).
- [135] J. Zou *et al.*, J. Appl. Phys. **105**, 013714 (2009).
- [136] J. Zou *et al.*, J. Appl. Phys. **101**, 033126 (2007).
- [137] J. Grames *et al.*, Phys. Rev. ST Accel. Beams **14**, 043501 (2011).
- [138] M. Reiser, *Theory and Design of Charged Particle Beams, 2nd Edition* (Wiley-VCH Verlag & Co. KGaA, Weinheim, New-York, 2008), Beam Physics and accelerator technology.
- [139] <http://www.srim.org> (accessed: 8 Feb 2019).
- [140] W. Liu *et al.*, Appl. Phys. Lett. **109** (2016).
- [141] K. L. Jensen *et al.*, J. Appl. Phys. **99**, 124905 (2006).
- [142] M. Gaowei *et al.*, Phys. Rev. Accel. Beams **22**, 073401 (2019).
- [143] M. Gaowei *et al.*, Appl. Phys. Lett. **5**, 116104 (2017).

## Figure captions

**Fig. 7.1** The three step model of photoemission can be used both for metals and semiconductors; here the parameters of copper and Cs<sub>2</sub>Te are compared.  $\lambda_{e-e}$  and  $\lambda_{e-p}$  correspond to the electron mean free path between electron-electron and electron-phonon scattering events;  $\tau$  is the electron extraction time (colored figure). Note that, even if an electron has total-energy  $E$  above the threshold level, it cannot escape unless the energy associated with its motion normal to the surface is also above the threshold level

**Fig. 7.2** Densities of states  $N(E)$  for a transition metal (Nb, top) and a p-band emitter (Pb, bottom), as functions of total-energy  $E$  measured from the base of the conduction band. The separation of filled and empty states is labeled by the Fermi energy, and the minimum energy required to escape the material (in the absence of the Schottky effect) is labeled as the threshold energy [6, 7] (colored figure). This threshold energy is the sum of the Fermi energy and the work function

**Fig. 7.2** Densities of states  $N(E)$  for a transition metal (Nb, top) and a p-band emitter (Pb, bottom), as functions of total-energy  $E$  measured from the base of the conduction band. The separation of filled and empty states is labeled by the Fermi energy, and the minimum energy required to escape the material (in the absence of the Schottky effect) is labeled as the threshold energy [6, 7] (colored figure). This threshold energy is the sum of the Fermi energy and the work function

**Fig. 7.3** Schematic representation of the link between the theoretical parameters controlling the QE of copper and macroscopic properties as well as ways to act on these properties

**Fig. 7.4** QE of a copper photocathode versus the applied electric field during 4 days of operation. Laser pulses at 266 nm with 6  $\mu$ J energy per pulse, at 10 Hz repetition rate, were used to illuminate the copper photocathode with quasi-normal incidence. The copper photocathode (inset) was diamond turned, providing an average roughness of a few nanometers. The theoretical curve corresponds to the QE expression (7.2) taken from [9]

**Fig. 7.5** Quantum efficiency of various metal photocathodes measured in a diode gun (350 kV and variable gap) using 6 ps rms laser pulses at 266 nm, and 10 Hz repetition rate. Cathode samples were exposed to air without any in-vacuum cleaning treatment [13].

**Fig. 7.6** QE variation of copper versus work function using light at 253 nm

**Fig. 7.7** Micrographs of a copper photocathode under white light illumination [17]

**Fig. 7.8** Quantum efficiency of a copper photocathode versus the illumination wavelength, from [25]

**Fig. 7.9** Effect of annealing a copper photocathode: QE (top) and temperature cycle (bottom) versus time for three samples [28]

**Fig. 7.10** Comparison of three-step model theory with LCLS Cu cathodes cleaned via laser cleaning and hydrogen-ion cleaning. (Color Figure)

**Fig. 7.11** QE map revealing the effect of laser illumination on QE degradation. Long term illumination has the effect of cracking organic molecules which then bind to the surface (source: [28]) (Color Figure)

**Fig. 7.12** Top: Surface profilometry of a diamond turned copper sample 2.7 mm by 1.5 mm (forged copper). Bottom: Transverse profile along the line shown in the top figure; grain size: 300  $\mu\text{m}$ ; roughness (Ra)  $\sim 3$  nm; height (peak-to-valley)  $\sim 30$  nm (source: [17]) (Color figure)

**Fig. 7.13** Atomic force microscope picture of diamond turned aluminum samples. The rms roughness is equal to 1.2 nm for this sample despite some local tips as high as 37 nm

**Fig. 7.14** A quasi half-cycle THz pulse is used to trigger optical field emission from a ZrC tip. The time structure of the current pulse is limited by the scope bandwidth, but should in principle follow the THz half-cycle

**Fig. 7.15** Top: Emitted current pulse when only a nanosecond long voltage pulse is applied (pure field emission). Bottom: Current pulse when a voltage pulse (ns) and a laser pulse (ps) are simultaneously applied. The cathode is a ZrC tip [43]

**Fig. 7.16** QE vs photon energy for lead and niobium photocathodes. The vertical line represents the threshold energy for lead at zero electric field

**Fig. 7.17** Overview of semiconductor photocathodes - QE versus illumination wavelength (Courtesy of Hamamatsu K. K. [47])

**Fig. 7.18** Evolution of the Cs evaporation current (related to the deposition rate) and collected photocurrent under constant illumination at 266 nm and while Te is deposited at 0.03 Å/s. Pressure rises to  $10^{-8}$  mbar ( $10^{-6}$  Pa) during deposition

**Fig. 7.19** Evolution of QE with time for various copper and Cs<sub>2</sub>Te photocathodes operating under the same conditions: extracting field 52 MV/m, 262 nm laser pulses of 4 ps rms duration at 10 Hz repetition rate, with  $10^{-9}$  mbar ( $10^{-7}$  Pa) photogun vacuum.

**Fig. 7.20** QE map of a Cs<sub>2</sub>Te photocathode measured inside the gun by scanning a small laser spot with constant energy.

**Fig. 7.21** Typical lifetime of Cs<sub>2</sub>Te photocathodes used in an RF photoinjector: Illumination with trains of 2400 laser pulses of ps duration during an 800 μs macropulse at 10 Hz, 262 nm illumination, 40 MV/m, 700 pC/pulse (source: [62])

**Fig. 7.22** Spectral response of a K<sub>2</sub>CsSb photocathode grown by ternary co-evaporation with in situ X-ray fluorescent monitoring

**Fig. 7.23** XRD evolution of sequential K<sub>2</sub>CsSb growth, showing the crystallization of the antimony film at 4 nm thick. This is followed by potassium deposition which causes the film to go amorphous at ~6000 s into the deposition. When the film recrystallizes into potassium antimonide, the QE (top plot) begins to rise

**Fig. 7.24** (Left) Energy level diagram of GaAs at the center of the Brillouin zone: a “close-up” view near the valence band maxima/conduction band minima, and (right) simplified view showing the optical transitions between sublevels for right circularly polarized light (solid lines) and left circularly polarized light (dashed lines), with relative transition strengths given by circled numbers

**Fig. 7.25** Energy level diagrams describing the formation of the negative electron affinity (NEA) condition on GaAs.  $E_{CB}$ ,  $E_F$ ,  $E_{VB}$ , and  $E_{vac}$  describe the conduction band base energy, the Fermi level, the valence band maximum energy and the local vacuum energy level, respectively.  $EA$  and  $EA_{eff}$  refer to the local electron affinity, and the latter determines the so-called “surface work function”  $\phi_s$  defined by  $\phi_s = E_{vac} - E_F$ .  $V_{dipole}$  is the further decrease in effective electron affinity caused by the CsF activation layer. The diagrams show: (a) intrinsic GaAs; (b) how p-type dopant lowers the Fermi level which—together with the negative applied external field and (in some cases) other effects—leads to downwards band bending at the surface; and (c) how adding a CsF layer lowers the surface potential-energy barrier and leads to further band bending, to a lower surface work function, and to the desired NEA condition.

**Fig. 7.26** Temperature dependence of the spin relaxation rate for the DP mechanism, BAP mechanism and the total value in bulk GaAs

**Fig. 7.27** The QE and ESP of bulk GaAs (100 cleave plane) with different Zn dopant densities, and measured at 300 K (left) and 77 K (right). Error bars are statistical. Axes ranges were kept identical to highlight the measurement variations observed between conditions. The bandgap energy  $E_g$  could be discerned for samples at 77 K (note arrow)

**Fig. 7.28** Maximum ESP versus sample temperature and dopant density (the wavelength of illumination was allowed to vary to provide peak polarization). Fits were applied using the sum of expressions (7.4) and (7.6), which describe the DP and BAP spin relaxation mechanisms, respectively. Vertical error bars are statistical; horizontal error bars relate to uncertainty in sample temperature

**Fig. 7.29** Schematic structure of the photocathodes: without DBR (left) and with DBR (right)

**Fig. 7.30** Calculated values of absorption, reflectivity and transmittance of the DBR photocathode, as a function of wavelength. Also shown, calculated QE and the QE enhancement factor compared to the photocathode without the DBR

**Fig. 7.31** (a) The QE and electron-spin polarization (ESP) for the strained GaAs/GaAsP superlattice photocathodes with and without DBR as a function of the wavelength; (b) Reflectivity and QE enhancement factor of DBR photocathode as a function of the wavelength. The dashed line indicates the resonant position

**Fig. 7.32** Electron impact ionization cross section for hydrogen molecules - the dominant gas species inside modern DC high voltage photoguns - as a function of electron kinetic energy

**Fig. 7.33** (Left) Hydrogen ion distribution and (right) vacancy distribution within GaAs, for different hydrogen ion energies. All simulations performed using the same hydrogen ion dose of  $8.1 \times 10^5$  nA · s. Plots obtained using SRIM [139]

**Fig. 7.34** Schematic representations of the GaAs crystal for three surface cleave planes, looking normal to the surface – from left to right, (100), (110) and (111). The red boxes denote the recurring geometric cells used for calculating the atomic number density for each cleave plane and  $a$  is the GaAs lattice constant.

**Fig. 7.35** Photocathode QE versus laser wavelength for commercial bulk GaAs samples with different surface cleave planes, prior to ion implantation

**Fig. 7.36** Typical QE maps of the photocathode obtained by scanning a focused low power green laser beam across the photocathode following activation. These maps show the bulk GaAs (111A) sample. Left: after the third activation following implantation with 100 V hydrogen ions. Right: after the third activation following implantation with 10 kV hydrogen ions. The 2-dimensional plots help to illustrate ion implantation uniformity: 100 V hydrogen ions were uniformly distributed across the entire sample but 10 kV hydrogen ions were focused to a region denoted by the ellipse, consistent with the particle tracking code simulations

**Fig. 7.37** QE versus heat cycle for bulk GaAs with three different surface cleave planes. Black Square: no implantation; Red Circle: implantation with 100 V hydrogen ions; Blue Triangle: implantation with 10 kV hydrogen ions. Error bars represent the standard deviation in QE values averaged over the entire sample for “no implantation”: and 100 V results, and over the small region denoted by the red circle in Fig. 7.36 (right) for the 10 kV results. Error bars are smaller than the data-point symbols for “no implantation” and 100 V results, because QE was very uniform across the sample. Heat cycles were: number 1: 250 °C for 20 minutes; 2: 370 °C for 30 minutes; 3: 490°C for 1 hour; 4 and 5: 550 °C for 1 hour

**Fig. 7.38** QE ratio, for samples implanted with 10 kV hydrogen ions to samples that were not exposed to hydrogen ions, as a function of heat cycle, for bulk GaAs with three different surface cleave planes. Heat cycle numbers: 1: 250 °C for 20 minutes; 2: 370 °C for 30 minutes; 3: 490 °C for 1 hour; 4 and 5: 550° C for 1 hour